Earth and Planetary Science Letters 506 (2019) 476–492

Contents lists available at ScienceDirect

Earth and Planetary Science Letters

www.elsevier.com/locate/epsl

Evidence for magma–evaporite interactions during the emplacement of the Central Atlantic Magmatic Province (CAMP) in Brazil

Thea H. Heimdal [a,*], Sara Callegaro [a], Henrik H. Svensen [a], Morgan T. Jones [a], Egberto Pereira [b], Sverre Planke [a,c]

[a] Centre for Earth Evolution and Dynamics (CEED), University of Oslo, PO Box 1028, Blindern, NO-0315 Oslo, Norway
[b] Department of Stratigraphy and Paleontology, Rio de Janeiro State University, Rio de Janeiro, Brazil
[c] Volcanic Basin Petroleum Research, Oslo Innovation Center, N-0349 Oslo, Norway

ARTICLE INFO

Article history:
Received 15 June 2018
Received in revised form 7 November 2018
Accepted 9 November 2018
Available online 26 November 2018
Editor: D. Vance

Keywords:
Central Atlantic Magmatic Province
end-Triassic mass extinction
sills
volcanic basins
magma–evaporite interactions

ABSTRACT

Mafic sills of the Central Atlantic Magmatic Province (CAMP) in Brazil are temporally linked to the end-Triassic extinction (ETE), one of the largest mass extinctions of the Phanerozoic. The sills were emplaced into the volatile-rich sedimentary rocks of the Amazonas and Solimões basins in northern Brazil. Here we present a new geochemical study of 26 dolerite samples from 6 deep boreholes in the Brazilian basins, including whole-rock major and trace elements, whole-rock Sr–Nd isotopes and detailed biotite mineral chemistry. The bulk of the dolerites are characterized by phenocrysts of clinopyroxene and plagioclase in subophitic to intergranular textures, Fe–Ti oxides, and rare olivine and orthopyroxene. A different mineralogical assemblage (microphenocrysts of alkali-feldspar, quartz, biotite and apatite) is found in small independent domains, localized within the framework of coarser plagioclase and clinopyroxene laths. These fine-grained evolved domains crystallized in late-stage, evolved melt pockets in the interstitial spaces between earlier crystallized coarser grained crystals. The majority of the studied dolerites are generally evolved tholeiitic basalts and basaltic andesites with low TiO_2 concentrations (<2.0 wt.%). Four samples have high TiO_2 concentrations (>2.0 wt.%), and are found in the eastern part of the Amazonas Basin. Whole-rock major and trace element and Sr–Nd isotope geochemistry of both low- and high-Ti sills is similar to that of previously published CAMP rocks from the two magma types. Low-Ti sills show enriched isotopic signatures ($^{143}Nd/^{144}Nd_{201Ma}$ 0.51215 to 0.51244; $^{87}Sr/^{86}Sr_{201Ma}$ 0.70568 to 0.70756), coupled with crustal-like characteristics in the incompatible element patters (e.g. depletion in Nb and Ta). Unaltered high-Ti samples show more depleted isotopic signatures ($^{143}Nd/^{144}Nd_{201Ma}$ 0.51260 to 0.51262; $^{87}Sr/^{86}Sr_{201Ma}$ 0.70363 to 0.70398). Low-Ti dolerites from both the Amazonas and Solimões basins contain biotite with extremely high Cl concentrations (up to 4.7 wt.%). We show that there is a strong correlation between host-rock lithology and Cl concentrations in biotite from the dolerites, and interpret this to reflect large-scale crustal contamination of the low-Ti magmas by halite-rich evaporites. Our findings support the hypothesis that sill-evaporite interactions increased volatile release during the emplacement of CAMP. This strengthens the case for active involvement of this LIP in the end-Triassic crisis, and suggests that the sub-volcanic part of a LIP can be of major importance in driving climate change and mass extinctions.

© 2018 Elsevier B.V. All rights reserved.

1. Introduction

A temporal link between Large Igneous Provinces (LIPs) and biotic upheavals is well documented throughout Earth history, and this applies to four of the 'big five' global mass extinction events of the Phanerozoic (Wignall, 2001; Bond and Wignall, 2014). However, beyond a geochronological link, the causal association between LIPs and mass extinctions remains debated. This is also the case for the Central Atlantic Magmatic Province (CAMP), which has been temporally linked to the end-Triassic extinction (ETE) and associated carbon cycle perturbations (Marzoli et al., 1999; Blackburn et al., 2013; Davies et al., 2017; Lindström et al., 2017; Heimdal et al., 2018). In general, release of volatile elements such as C, S and halogens, during the emplacement of LIPs is often suggested as a mechanism to explain environmental changes and mass extinctions. While the release of carbon-containing gases may re-

* Corresponding author.
E-mail address: t.h.heimdal@geo.uio.no (T.H. Heimdal).

https://doi.org/10.1016/j.epsl.2018.11.018
0012-821X/© 2018 Elsevier B.V. All rights reserved.

sult in global warming, SO_2, HCl and HF could lead to significant environmental stress, through toxicity, acid rain, cooling and/or ozone depletion (e.g. Wignall, 2001; Bond and Wignall, 2014; Jones et al., 2016). Understanding the processes behind volatile generation and release during LIP activity is therefore of great importance for constraining subsequent environmental perturbations.

In addition to lava degassing, interactions between sub-volcanic intrusives and volatile-rich host-rocks in large-scale volcanic basins may significantly increase volatile release during LIP emplacement, through contact metamorphism and/or contamination of the magma. This has been documented for the Emeishan and Siberian Traps LIPs, which are temporally linked to the end-Guadalupian and end-Permian mass extinctions, respectively (Ganino and Arndt, 2009; Svensen et al., 2009; Pang et al., 2013; Black et al., 2013). The volume and speciation of sediment-derived volatiles are heavily influenced by the composition of the host-rock, and devolatilization is particularly effective when shale, evaporite, limestone, coal and/or hydrocarbon-bearing strata are intruded (Svensen et al., 2004, 2009; Ganino and Arndt, 2009; Aarnes et al., 2011). In the case of the CAMP, thermal modeling has shown that up to 88,000 Gt CO_2 could have been generated from contact metamorphism of limestone and organic-rich shale during the emplacement of sills in the Amazonas and Solimões basins (Fig. 1a; Heimdal et al., 2018). These sills have been temporally linked to the ETE by high-precision U–Pb dating (Davies et al., 2017; Heimdal et al., 2018), and constitute a large-scale intrusive complex within these basins, being particularly prevalent in evaporite-bearing host-rocks (Fig. 1b–c).

Interactions between magmas and evaporites, including the incorporation of sedimentary pore fluids (e.g. brines), can significantly increase volatile contents of magmas. Corroborating evidence includes 1) high Cl, F, and S concentrations in melt inclusions (Sobolev et al., 2009; Black et al., 2013), and high bulk-rock S concentrations and $\delta^{34}S$ values (Ripley et al., 2003; Li et al., 2009) in intrusives emplaced in evaporite host-rocks, 2) high Cl contents in matrix glasses of submarine basalts (e.g. Michael and Schilling, 1989; Coombs et al., 2004), and 3) experimental data showing high S and Cl concentrations in mafic and ultramafic magmas in the presence of evaporite or brines (Chevychelov and Suk, 2003; Iacono-Marziano et al., 2017).

Here, the aim is to investigate potential interactions between CAMP magmas and sedimentary host-rocks in the Amazonas and Solimões basins (Brazil). Magma contamination by sedimentary rocks may be reflected by enrichment in whole-rock $^{87}Sr/^{86}Sr$ ratios, incompatible Large Ion Lithophile Elements (LILE) concentrations and/or high halogen (e.g. Cl, F) contents in halogen-bearing minerals. Available geochemical and isotopic data from the Brazilian dolerite sills are sparse (Alves and Rodrigues, 1985; De Min et al., 2003; Wanderley Filho et al., 2006), likely due to limited outcrops and difficulties in obtaining borehole samples. We present new whole-rock geochemical and Sr–Nd isotopic data, as well as biotite compositions, from 26 dolerite samples from 6 individual boreholes (Fig. 1b). We compare the whole-rock geochemistry and isotope data with published data from other CAMP intrusives and lavas, aiming to constrain the extent and modes of interaction between Brazilian CAMP sills and their host-rocks.

2. CAMP in Brazil and the Amazonas and Solimões basins

CAMP intrusive and extrusive rocks are found in a number of onshore sedimentary basins in Brazil, including the Amazonas, Solimões, Acre, Maranhao–Parnaíba, Anarí and Tapirapuá, as well as in the Guyana cratonic block in NE Brazil (Milani and Zalán, 1999; De Min et al., 2003;Wanderley Filho et al., 2006; Merle et al., 2011; Klein et al., 2013). Most of these rocks have TiO_2 concentrations <2.0 wt.%, and fall within the low-Ti group determined for CAMP rocks following Marzoli et al. (1999). High-Ti rocks (TiO_2 > 2.0 wt.%) occur in the N–NE parts of Brazil, including some of the Cassiporé dykes (De Min et al., 2003), Marañhao lava flows (Merle et al., 2011), Parnaíba dykes (Klein et al., 2013) and Amazonas sills (Davies et al., 2017; Heimdal et al., 2018). Previous studies have shown that the high- and low-Ti magma types cannot be derived from one another by either closed- or open-system magmatic evolution, suggesting that they derive from different mantle sources. While the low-Ti CAMP magmas are suggested to derive from a lithospheric mantle enriched by recycled crust, high-Ti magmas originated from the asthenosphere and were enriched by melts derived from metasomatic veins (cf. Marzoli et al., 2018 and references therein).

CAMP magmatism is particularly widespread as sill intrusions in the vast Amazonas and Solimões basins ($\sim 1 \times 10^6$ km^2; Wanderley Filho et al., 2006), and these have been suggested to represent up to 70% of the total CAMP sill volume (Svensen et al., 2018). Sills from the Amazonas Basin have previously been described as low-Ti tholeiitic basalts and andesitic basalts (De Min et al., 2003), and sills from both basins are generally characterized by a mineral assemblage of clinopyroxene, plagioclase, Fe–Ti oxides, rare olivine and orthopyroxene and accessory quartz–feldspar intergrowths. Recent studies report the presence of high-Ti sills in the eastern part of the Amazonas Basin (Davies et al., 2017; Heimdal et al., 2018), but no high-Ti occurrences have been observed for the Solimões Basin. High-precision U–Pb geochronology of four dolerites from the Amazonas and Solimões basins (including two samples used in this study) demonstrate that they overlap in age, with U–Pb ages for low-Ti dolerites of 201.525 ± 0.065 (Amazonas Basin) and 201.470 ± 0.089 (Solimões Basin), and for high-Ti dolerites in the Amazonas Basin of 201.477 ± 0.062 and 201.364 ± 0.023 (Davies et al., 2017; Heimdal et al., 2018). This suggests that low- and high-Ti CAMP magmatism were active simultaneously, although low-Ti magmatism likely started earlier.

The sedimentary rocks intruded by sills in the Amazonas and Solimões basins include a lower (Ordovician–Mississippian) and upper (Pennsylvanian–Permian) Paleozoic series (Fig. 1b–c; Milani and Zalán, 1999). The lower Paleozoic series consists of sandstones and shales, some of which are particularly organic-rich (total organic content up to 8 wt.%; Milani and Zalán, 1999; Gonzaga et al., 2000). The upper Paleozoic series is dominated by evaporite and carbonate deposits of varying relative abundances, interlayered with clastic rock. Sills are widespread within the upper Paleozoic series, extending almost continuously from the western margin of the Solimões Basin to the eastern margin of the Amazonas Basin (Fig. 1c). Sills within the lower Paleozoic unit are restricted to the eastern part of the Amazonas basin (Fig. 1c). As illustrated in Fig. 1b–c, high-Ti sills are found only in the lower Paleozoic series.

3. Materials and methods

The sample material includes 26 cores or drilling chips of dolerite from 6 deep boreholes (Table 1; Supplementary Fig. S1). From the Amazonas Basin, we studied 18 samples collected from 5 boreholes (ATZ, OAST, MA, IB and IBST), representing 12 individual sills. In addition, we studied 8 samples from the Solimões Basin (termed SOL hereinafter), but the borehole log(s) is not available, and thus the sample depths, borehole location(s) and number of sills sampled are not known. Note that borehole IBST was interrupted and borehole IB was drilled a few kilometers from IBST in the same river margin (Fig. 1a), thus samples IB-990 and IBST-991 (Fig. 1b) most likely represent the same sill.

Only visually un-altered dolerite was cut from the cores. For the drilling chips, the smallest fractions (<1 mm) were removed by sieving, before dolerite fragments were handpicked using an optical microscope, and washed in an ultrasonic bath.

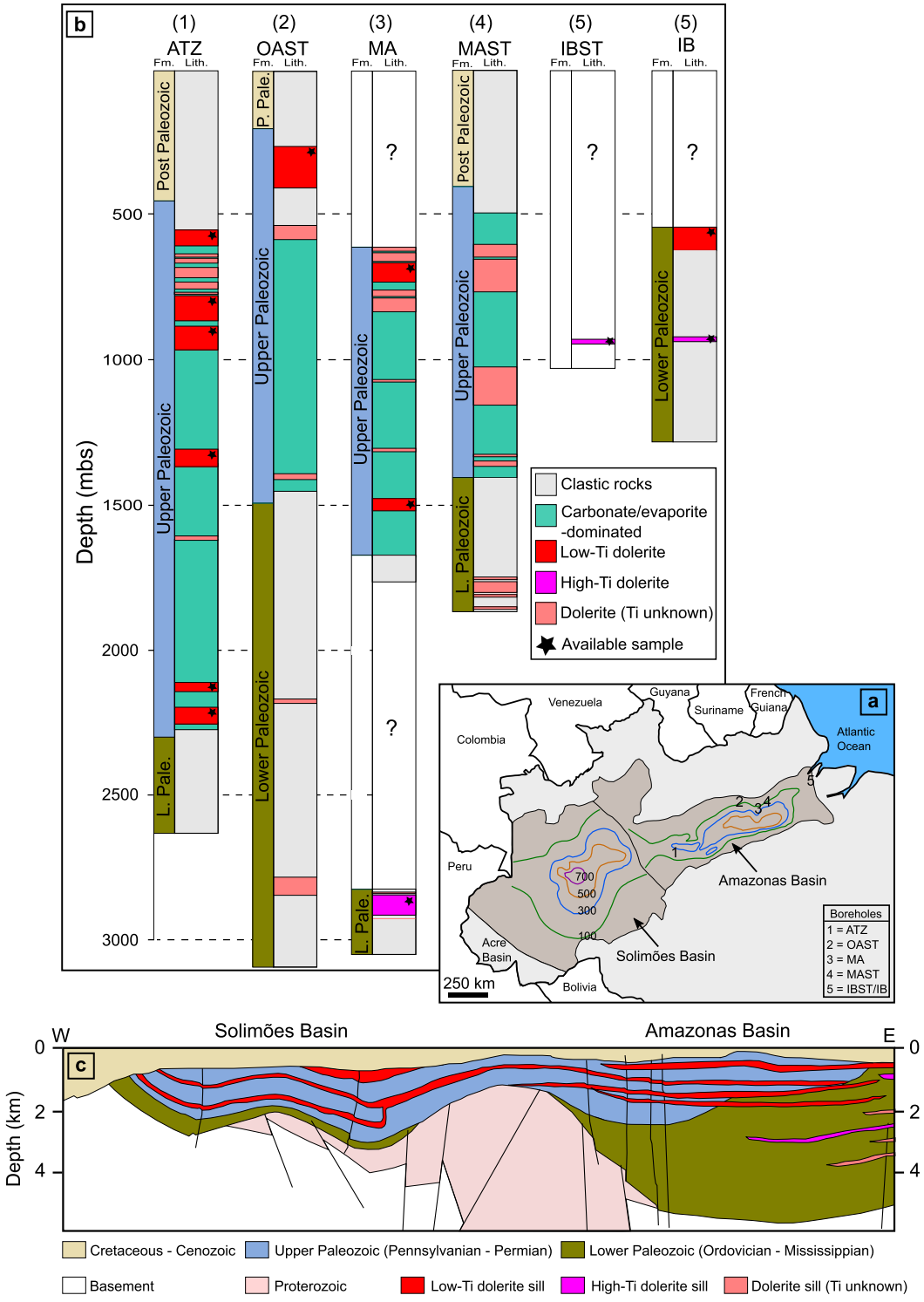

Fig. 1. (a) Map showing the location of the Amazonas and Solimões sedimentary basins in northern Brazil (redrawn after Heimdal et al., 2018). Colored contour lines represent the cumulative sill thickness, which peaks in the central parts of the basins and decreases toward the margins, and show that the sills are distributed throughout a large area of both basins. Numbers 1 to 5 represent borehole locations, and correspond to the numbers shown above the boreholes in (b). Note that the location of borehole SOL (drilled in the Solimões Basin) is not known. (b) Boreholes from the Amazonas Basin (ordered from W to E). The majority of dolerites have low TiO_2 concentrations (<2 wt.%; red color) and have intruded the upper Paleozoic section, which is dominated by evaporite and carbonate (interlayered with clastic sediments). Boreholes with known stratigraphy show that sills with high TiO_2 concentrations (>2.0 wt.%; purple color) are restricted to the lower Paleozoic section. Sills with unknown TiO_2 concentrations are marked in pink. Numbers 1 to 5 represent borehole locations (shown in (a). Note that the location of borehole SOL (drilled in the Solimões Basin) is not known and the borehole log is not provided. Borehole IB is a continuation of borehole IBST a few kilometers apart, thus the high-Ti sills recorded at around 990 m depth in these boreholes likely represent the same sill. Sills with available sample material, which have been analyzed in this study, are marked by a star symbol. Mbs. = meters below surface. Fm. = formation, Lith. = lithology, P. Pale. = Post Paleozoic, L. Pale. = Lower Paleozoic. (c) Schematic cross-section of the Solimões and Amazonas basins (redrawn after Heimdal et al., 2018 and based on sill and formation depths from boreholes in (a) shows that sills are widespread in upper Paleozoic rocks (dominated by evaporite and carbonate, interlayered with clastic rocks), extending almost continuously from the eastern margin of the Amazonas Basin to the western margin of the Solimões Basin. Sills within lower Paleozoic sedimentary rocks are restricted to the eastern part of the Amazonas Basin. (For interpretation of the colors in the figure(s), the reader is referred to the web version of this article.)

Table 1
Whole-rock major (wt.%) and trace (ppm) element concentrations and Sr–Nd isotopic data of dolerites from the Amazonas and Solimões basins.

Borehole	SOL	SOL	SOL	SOL	SOL	SOL	SOL	SOL	MA	MA	ATZ	ATZ	ATZ
Sample	SOL-1	SOL-2	SOL-3	SOL-4	SOL-5	SOL-6	SOL-7	SOL-8	690-705	1490-1508	558-603	801-837	837-855
Depth (mbs)	na	na	na	na	na	na	na	na	690-705	1490-1508	558-603	801-837	837-855
Basin	SO	SO	SO	SO	SO	SO	SO	SO	AM	AM	AM	AM	AM
Sample type	Drill chips	Drill chips	Drill chips	Drill chips	Drill chips	Drill chips	Drill chips	Drill chips	Drill chips	Drill chips	Drill chips	Drill chips	Drill chips
TiO_2 content	Low-Ti	Low-Ti	Low-Ti	Low-Ti	Low-Ti	Low-Ti	Low-Ti	Low-Ti	Low-Ti	Low-Ti	Low-Ti	Low-Ti	Low-Ti
TAS classification	Bas. and.	Bas. and.	Bas. and.	Basalt	Bas. and.	Basalt	Bas. and.	Basalt	Bas. and.	Bas. and.	Basalt	Basalt	Basalt
Intruded lithology	E/L	E/L	E/L	E/L	E/L	E/L	E/L	E/L	E/L	E/L	E/L	E/L	E/L
SiO_2 (wt.%)	52.31	52.92	52.79	51.76	52.35	50.31	53.03	51.55	52.61	52.93	51.45	51.09	51.1
TiO_2	1.23	1.41	1.25	1.11	1.62	0.73	0.85	0.67	1.17	1.26	1.42	1.12	1.24
Al_2O_3	14.81	13.6	14.31	14.07	13.7	14.78	14.49	15.33	14.67	14.68	14.27	14.53	13.95
Fe_2O_3	11.15	12.30	11.23	11.93	13.36	9.29	10.73	8.26	10.75	11.50	11.72	10.12	11.68
MnO	0.20	0.19	0.16	0.19	0.20	0.15	0.17	0.14	0.17	0.17	0.18	0.17	0.18
MgO	5.88	5.30	6.33	7.46	5.37	9.62	6.71	7.89	6.01	5.56	6.10	6.83	6.06
CaO	8.58	8.77	9.76	10.61	9.97	13.83	11.34	13.92	9.94	9.75	9.24	11.28	10.22
Na_2O	3.01	2.7	3.08	2.24	2.65	1.5	2.37	1.78	2.47	2.63	2.67	2.63	2.77
K_2O	0.91	0.92	0.61	0.57	0.7	0.26	0.53	0.36	0.67	0.8	0.54	0.43	0.56
P_2O_5	0.12	0.16	0.14	0.12	0.16	0.07	0.12	0.08	0.16	0.15	0.16	0.10	0.11
L.O.I.	2.4	1.1	1.1	0.7	0.4	0.0	0.3	0.1	1.8	1.2	2.2	1.3	0.9
Total	100.6	99.4	100.8	100.7	100.5	100.5	100.7	100.1	100.4	100.6	99.95	99.57	98.75
Mg#	55	50	56	59	48	70	59	68	56	52	54	61	54
Sc (ppm)	36	36	39	39	41	41	40	39	37	36	37	38	37
V	313	332	340	312	411	252	256	223	297	316	360	303	323
Cr	80	60	90	80	150	860	130	610	180	60	90	230	90
Co	39	43	39	47	43	42	43	38	40	40	38	37	36
Ni	60	60	60	100	60	180	60	110	80	60	80	80	70
Cu	150	140	120	130	170	80	100	80	110	130	150	80	100
Zn	90	110	70	100	100	50	70	60	90	80	70	90	90
Ga	19	19	19	17	19	14	17	15	18	18	19	18	18
Ge	1.6	1.5	1.5	1.5	1.5	1.6	1.5	1.6	1.5	1.5	1.6	1.4	1.5
Rb	24	29	20	17	20	8	16	11	17	25	14	11	14
Sr	227	254	245	215	231	157	198	173	250	223	208	220	216
Y	22.7	27.1	25.9	21.6	28.9	13.7	20.8	15.5	23.5	25	25.6	21.4	24.5
Zr	94	116	94	82	111	45	76	55	100	104	105	81	96
Nb	6	7.1	6.3	5.2	6.3	2.5	4.7	3.3	6.1	6.1	6.8	5.3	6.1
Cs	0.8	1	0.7	0.6	0.6	0.3	0.5	0.3	0.4	1	0.4	0.3	0.4
Ba	200	285	191	176	195	141	140	103	220	225	152	144	185
Hf	2.8	3.1	2.7	2.3	3.1	1.3	2	1.5	2.8	3	3	2.3	2.7
Ta	0.43	0.52	0.45	0.36	0.47	0.19	0.34	0.24	0.43	0.43	0.5	0.37	0.45
Th	2	2.58	2.03	1.53	2.04	0.76	1.7	1.16	2.21	2.34	1.93	1.49	1.91
U	0.75	0.71	0.48	0.39	0.52	0.2	0.45	0.29	0.54	0.62	1.62	0.37	0.51
La	10.3	15.3	9.17	9.01	11.7	4.16	8.28	5.39	12.3	13.4	11.2	7.68	9.15
Ce	23.2	33.2	21.9	20.2	26.9	9.99	18.8	12.8	27.2	30.1	26.2	18.8	22
Pr	3.12	4.16	2.95	2.71	3.7	1.48	2.5	1.73	3.5	3.81	3.52	2.56	2.98
Nd	13.8	18	13.5	12.1	16.4	6.9	11.2	8.06	15.6	16.6	16.1	11.4	14
Sm	3.54	4.44	3.76	3.29	4.67	2.04	2.98	2.15	3.85	4.03	4.04	3.2	3.73
Eu	1.15	1.43	1.26	1.14	1.44	0.73	1	0.8	1.28	1.33	1.33	1.05	1.28
Gd	3.94	4.97	4.31	3.79	5.11	2.29	3.5	2.6	4.24	4.68	4.69	3.6	4.19
Tb	0.65	0.82	0.75	0.63	0.85	0.41	0.6	0.45	0.71	0.75	0.78	0.62	0.72
Dy	4	4.87	4.6	3.95	5.13	2.53	3.67	2.75	4.21	4.51	4.78	3.92	4.47
Ho	0.81	0.97	0.93	0.8	1.04	0.52	0.71	0.55	0.83	0.9	0.95	0.77	0.88
Er	2.27	2.78	2.68	2.32	2.97	1.5	2.05	1.58	2.38	2.71	2.66	2.2	2.45
Tm	0.341	0.4	0.395	0.334	0.429	0.211	0.302	0.223	0.343	0.381	0.376	0.313	0.361
Yb	2.2	2.51	2.47	2.1	2.77	1.28	1.98	1.37	2.12	2.44	2.42	1.98	2.37
Lu	0.336	0.387	0.382	0.327	0.437	0.196	0.301	0.205	0.323	0.378	0.365	0.302	0.353
$^{87}Rb/^{86}Sr$	0.298360	0.322172	0.230348	0.223106	0.244296	0.143765	0.228016	0.179409	0.191876	0.316344	0.189923	0.141077	0.182881
$^{147}Sm/^{144}Nd$	0.161932	0.155708	0.175821	0.171643	0.179759	0.186640	0.167962	0.168390	0.155789	0.153250	0.158407	0.177201	0.168190
$^{87}Sr/^{86}Sr$	0.708399	0.707650	0.707566	0.707114	0.707061	0.706206	0.707336	0.707038	0.707407	0.707684	0.707403	0.706780	0.706973
±2S	0.000009	0.000008	0.000008	0.000009	0.000009	0.000008	0.000007	0.000009	0.000009	0.000009	0.000009	0.000009	0.000008
$^{143}Nd/^{144}Nd$	0.512447	0.512375	0.512531	0.512528	0.512547	0.512595	0.512499	0.512496	0.512371	0.512405	0.512550	0.512571	0.512549
±2S	0.000006	0.000007	0.000006	0.000006	0.000006	0.000006	0.000006	0.000006	0.000006	0.000006	0.000006	0.000006	0.000006
$^{87}Sr_i/^{86}Sr$	0.707564	0.706749	0.706922	0.706490	0.706378	0.705804	0.706698	0.706536	0.706870	0.706799	0.706872	0.706385	0.706461
$^{143}Nd_i/^{144}Nd$	0.512234	0.512170	0.512300	0.512302	0.512311	0.512349	0.512278	0.512274	0.512166	0.512203	0.512342	0.512338	0.512328
εNd_i	−2.84	−4.08	−1.55	−1.50	−1.34	−0.58	−1.98	−2.04	−4.16	−3.43	−0.73	−0.81	−1.01

Table 1 (*continued*)

Borehole	ATZ	ATZ	ATZ	ATZ	ATZ	ATZ	ATZ	OAST	IB	IB	IBST	MA	MA
Sample	900-927	1311-1332	1332-1359	2106-2118	2121-2130	2200-2217	2220-2247	OAST	584	990	IBST	2883	2884
Depth (mbs)	900-927	1311-1332	1332-1359	2106-2118	2121-2130	2200-2217	2220-2247	382	584	990	991	2883	2884
Basin	AM	AM	AM	AM	AM	AM	AM	AM	AM	AM	AM	AM	AM
Sample type	Drill chips	Drill chips	Drill chips	Drill chips	Drill chips	Drill chips	Drill chips	Core	Core	Core	Core	Core	Core
TiO_2 content	Low-Ti	Low-Ti	Low-Ti	Low-Ti*	Low-Ti	Low-Ti	Low-Ti	Low-Ti	Low-Ti	High-Ti	High-Ti	High-Ti	High-Ti
TAS classification	Basalt	Basalt	Basalt	Basalt	Basalt	Basalt	Basalt	Basalt	Bas. and.	Basalt*	Picrobasalt*	Basalt	Basalt
Intruded lithology	E/L	E/L	E/L	E/L	E/L	E/L	E/L	Clastic	?	Clastic	Clastic	Clastic	Clastic
SiO_2 (wt.%)	51.24	51.46	51.82	na	50.82	51.94	51.62	50.98	53.22	42.96	38.22	47.32	46.42
TiO_2	1.05	1.04	0.77	na	1.37	1.40	1.25	1.07	1.17	3.30	3.24	2.21	2.41
ddocument Al_2O_3	13.69	13.98	14.94	na	13.3	13.98	14.55	15.76	14.95	15.28	14.5	13.52	12.82
Fe_2O_3	10.42	10.36	9.38	na	13.78	12.69	12.50	9.73	11.41	16.49	18.55	16.94	16.21
MnO	0.17	0.16	0.16	na	0.20	0.20	0.20	0.20	0.17	0.16	0.30	0.23	0.24
MgO	7.57	5.73	7.78	na	6.31	6.20	6.56	6.38	6.11	2.98	2.02	7.79	7.28
CaO	11.01	11.28	11.62	na	10.44	10.12	10.47	12.1	9.85	8.25	10.79	9.32	10.37
Na_2O	2.52	2.72	2.35	na	2.42	2.52	2.35	2.25	2.48	2.99	2.53	2.21	2.06
K_2O	0.58	0.77	0.54	na	0.54	0.63	0.61	0.41	0.71	0.44	0.29	0.37	0.26
P_2O_5	0.11	0.13	0.09	na	0.13	0.14	0.12	0.09	0.12	0.30	0.29	0.19	0.13
L.O.I.	2.1	3.0	0.7	na	0.4	0.5	0.4	1.4	0.5	6.6	8.2	-0.1	1.6
Total	100.4	100.6	100.1	na	99.68	100.3	100.7	100.3	100.7	99.79	98.88	100	99.8
Mg#	62	56	65	na	51	53	54	60	55	29	20	51	51
Sc (ppm)	39	35	36	na	42	43	43	38	37	48	44	31	38
V	285	257	228	na	389	397	358	300	307	627	636	479	549
Cr	410	110	330	na	60	110	80	190	40	150	160	300	260
Co	37	35	42	na	47	43	44	40	42	51	52	62	62
Ni	100	60	140	na	90	80	80	80	70	100	100	160	170
Cu	80	60	50	na	130	300	160	130	130	390	420	320	260
Zn	70	60	60	na	90	410	80	60	80	180	160	130	90
Ga	16	18	17	na	18	19	18	17	18	25	26	21	21
Ge	1.4	1.4	1.5	na	1.6	1.6	1.6	1.4	1.4	1.4	1.1	1.6	1.5
Rb	15	22	15	na	17	16	16	11	22	14	8	9	8
Sr	209	432	248	na	191	170	174	193	200	400	318	214	195
Y	22.1	23.6	19.3	na	26.9	28.6	24.9	19.4	22.5	36.3	43.3	23.9	23.6
Zr	86	98	73	na	94	102	86	73	96	228	202	104	101
Nb	5.7	6.1	4.1	na	5.5	5.8	5.1	4.7	5.6	12.7	13.5	7.4	7.2
Cs	0.3	0.7	0.5	na	0.8	0.8	0.9	0.5	0.9	1.6	1	1.2	1.6
Ba	164	226	184	na	123	113	125	116	232	384	252	99	68
Hf	2.5	2.8	2	na	2.7	3	2.4	2.1	2.7	5.6	5.8	3	2.9
Ta	0.4	0.44	0.3	na	0.36	0.42	0.39	0.34	0.43	0.95	0.97	0.51	0.48
Th	1.93	2.41	1.63	na	1.49	1.54	1.3	1.27	2.07	1.42	1.39	0.85	0.8
U	0.56	0.75	0.4	na	0.39	0.49	0.33	0.31	0.55	0.4	0.41	0.24	0.21
La	9.1	12	8.8	na	8.96	10.1	7.75	7.41	10.4	14.2	15.3	8.71	8.07
Ce	20.9	26.8	19.6	na	21.2	22.9	18.4	17.2	24	36.3	38.8	21.6	20.3
Pr	2.82	3.49	2.55	na	2.93	3.06	2.57	2.37	3.18	5.25	5.64	3.12	2.87
Nd	12.3	15	11.1	na	13.5	14.2	12.3	11.3	13.5	24.6	26.5	15	13.8
Sm	3.18	3.71	3.02	na	3.93	4.04	3.36	2.76	3.49	7	7.42	4.03	4.11
Eu	1.14	1.25	0.957	na	1.31	1.37	1.18	1.02	1.13	2.32	2.8	1.54	1.64
Gd	3.85	4.08	3.34	na	4.63	4.89	4.12	3.19	4.02	7.61	8.69	4.7	4.53
Tb	0.63	0.69	0.55	na	0.77	0.79	0.7	0.55	0.66	1.18	1.41	0.78	0.75
Dy	3.86	4.18	3.4	na	4.67	5	4.36	3.52	4.03	7.1	8.23	4.59	4.41
Ho	0.79	0.87	0.69	na	0.98	1.05	0.89	0.71	0.82	1.36	1.6	0.88	0.85
Er	2.22	2.41	1.96	na	2.85	3	2.47	1.97	2.38	3.73	4.35	2.37	2.37
Tm	0.321	0.352	0.287	na	0.405	0.436	0.359	0.291	0.344	0.526	0.614	0.328	0.339
Yb	2.06	2.26	1.83	na	2.54	2.82	2.34	1.87	2.2	3.25	3.92	2.06	2.18
Lu	0.316	0.359	0.274	na	0.391	0.43	0.371	0.28	0.331	0.467	0.597	0.321	0.327
$^{87}Rb/^{86}Sr$	na	0.143706	0.170666	na	0.251148	0.265552	0.259450	0.160803	0.310396	0.098787	0.071002	0.118630	0.115727
$^{147}Sm/^{144}Nd$	na	0.156128	0.171746	na	0.183775	0.179606	0.172451	0.154189	0.163193	0.179645	0.176771	0.169614	0.188024
$^{87}Sr/^{86}Sr$	na	0.707950	0.707271	na	0.707457	0.706594	0.706702	0.706127	0.707678	0.710159	0.709574	0.703960	0.704290
±2S	na	0.000009	0.000009	na	0.000008	0.000008	0.000009	0.000008	0.000007	0.000009	0.000009	0.000008	0.000008
$^{143}Nd/^{144}Nd$	na	0.512352	0.512390	na	0.512631	0.512645	0.512665	0.512582	0.512460	0.512878	0.512888	0.512843	0.512846
±2S	na	0.000006	0.000005	na	0.000006	0.000006	0.000006	0.000005	0.000006	0.000005	0.000005	0.000005	0.000006
$^{87}Sr_i/^{86}Sr$	na	0.707548	0.706793	na	0.706754	0.705851	0.705976	0.705677	0.706810	0.709883	0.709375	0.703628	0.703966
$^{143}Nd_i/^{144}Nd$	na	0.512147	0.512164	na	0.512389	0.512409	0.512438	0.512379	0.512245	0.512642	0.512655	0.512620	0.512599
εNd_i	na	−4.54	−4.20	na	0.20	0.58	1.15	0.00	−2.61	5.12	5.39	4.70	4.28

Major elements and Ba, Sc, Sr, V, and Zr are analyzed by ICP-OES, while the remaining trace elements are analyzed by ICP-MS. mbs = meters below surface. na = not available/analyzed. SO = Solimões Basin. AM = Amazonas Basin. Low-Ti = TiO_2 <2.0 wt.%. High-Ti = TiO_2 >2.0 wt.%. TAS = Total Alkali and Silica. Bas. and. = basaltic andesite. Low-Ti* = whole-rock major elements are not analyzed for this sample, however it is from the same dolerite sill as sample ATZ-2121/2130. Basalt/picobasalt* = highly altered sample. Black boxes indicate that the samples are from the same dolerite sill. E/L = evaporite/limestone; layers of evaporite and limestone with varying relative abundance, interlayered with clastic rock, where evaporite and limestone are the dominant lithologies. Mg# = 100 Mg/(Mg+Fe^{2+}), calculated for Fe^{3+}/Fe^{2+} = 0.15 following De Min et al. (2003). Nd and Sr isotopic ratios were corrected for mass fractionation using a $^{146}Nd/^{144}Nd$ ratio of 0.7219 and a $^{88}Sr/^{86}Sr$ ratio of 8.375209. Repeated measurements of the Strontium Carbonate Standard (SRM 987) at the time of analysis yielded an average $^{87}Sr/^{86}Sr$ ratio of 0.710234 ± 9 (2SD) (n = 7). The $^{87}Sr/^{86}Sr$ values presented in the table are adjusted for daily variations between the measured values of SRM 987 and the accepted $^{87}Sr/^{86}Sr$ value of this standard (0.710240). Repeated isotopic measurements of the La Jolla Reference Standard at the time of analysis yielded an average $^{143}Nd/^{144}Nd$ ratio of 0.511852 ± 7 (2SD) (n = 6). Given a reference value of $^{143}Nd/^{144}Nd$ = 0.511850 for the La Jolla standard, no further adjustments of sample values were undertaken. i = back-calculated isotopic ratios based on an age of 201 Ma. ±2S = uncertainty expressed as standard deviation at 2σ level.

Whole-rock major and trace element compositions were analyzed in 25 samples by Inductively Coupled Plasma Optical Emission (ICP-OES) or ICP Mass Spectrometry (ICP-MS) using the 4Lithores method by Activation Laboratories Ltd. Sample powders were mixed with a flux of lithium metaborate and tetraborate and fused in an induction furnace, before being mixed with 5% nitric acid until the samples were completely dissolved. Major elements and selected trace elements (Ba, Be, Sc, Sr, V and Zr) were analyzed by ICP-OES (Thermo Jarell-Ash ENVIRO II ICP or a Varian Vista 735 ICP), whereas the remaining trace elements were analyzed by ICP-MS (Perkin Elmer Sciex ELAN 6000, 6100 or 9000 ICP/MS). Along with the samples, certified reference materials, a method reagent blank, and sample replicates were also analyzed (Supplementary Tables S1–S2). Calibration was performed using six prepared USGS and CANMET certified reference materials for the ICP-OES analysis, and 12 for the ICP-MS analysis. For the ICP-OES analysis, one of the standards was used for every group of ten samples, while the ICP-MS instrument was recalibrated every 40 samples. Detection limits for all measured elements are reported in Supplementary Tables S1–S2. Analytical uncertainties for major elements are estimated at <5%, while for trace elements, uncertainties are 100% at the detection limit, 20% at 10 times the detection limit, and 10% at 100 times the detection limit.

Loss on Ignition (LOI) was determined by igniting sample powders in a chamber furnace at 1000 °C for 2 h, and weighing the samples before and after heating.

Whole-rock Sr–Nd isotopic compositions were determined for 24 samples using a Thermal Ionization Mass Spectrometer (TIMS; Finnigan MAT 262) at the Bergen Geoanalytical Facility, University of Bergen, following the procedures described in Pin et al. (1994). The pulverized samples were heated in a chamber furnace to 1000 °C for 1 h and decomposed in HF/HNO_3 in Savillex beakers on a heating plate. The dissolved and dried samples were taken up in 2 N HNO_3 prior to chromatographic separation. Sr and Nd were separated from matrix elements by ion selective extraction chromatography on three different chromatographic materials supplied by Eichrom. Rare Earth Elements (REE) were first retained on TRU Spec columns. In the next step the retained REE elements were purified on LN Spec resin in order to selectively recover Nd. After removal and recovery of REE, Sr was extracted from matrix effluent by the ion specific resin, Sr Spec. Nd and Sr isotopic ratios were corrected for mass fractionation using a $^{146}Nd/^{144}Nd$ ratio of 0.7219 and a $^{88}Sr/^{86}Sr$ ratio of 8.375209. Repeated measurements of the Strontium Carbonate Standard (SRM 987) at the time of analysis yielded an average $^{87}Sr/^{86}Sr$ ratio of 0.710234 ± 9 (2SD) ($n = 7$). $^{87}Sr/^{86}Sr$ sample values (presented in Table 1) were adjusted for daily variations between the measured values of SRM 987 and the accepted $^{87}Sr/^{86}Sr$ value of this standard (i.e. 0.710240). Repeated isotopic measurements of the La Jolla Reference Standard at the time of analysis yielded an average $^{143}Nd/^{144}Nd$ ratio of 0.511852 ± 7 (2SD) ($n = 6$), equivalent to the accepted reference value of 0.511850, and negated the need for further correction.

Mineral compositions were obtained from polished thin sections using a Cameca SX100 electron microprobe at the University of Oslo, operated in wavelength-dispersive (WDS) mode at 15 kV, 15 nA, with a focused electron beam and a counting time of 10 s on peak. Matrix corrections were performed according to the PAP procedure implemented in the Cameca software (Pouchou and Pichour, 1984). Calibration standards were as follows: wollastonite (Si, Ca), orthoclase (K), albite (Na), synthetic Al_2O_3 (Al), pure iron metal (Fe), pyrophanite (Mn, Ti) synthetic periclase (Mg), synthetic corundum (Cr), nickel oxide (Ni), synthetic alforsite (Cl), fluorite (F) and Durango apatite (Ca, P, F). Where possible, F, Cl, Na and K were analyzed first. In addition, backscatter electron images of the petrographic features were taken.

4. Results

4.1. Petrography

All dolerites have a phaneritic texture with mineral sizes varying from fine- to medium-grained. The bulk of the dolerites (Fig. 2a–b) show a subophitic to intergranular texture dominated by phenocrysts of augitic ($Wo_{42-22}En_{51-31}Fs_{46-9}$) and pigeonitic ($Wo_{13-6}En_{71-39}Fs_{51-21}$) clinopyroxene and plagioclase ($An_{85-36}Ab_{61-15}Or_{3-0.2}$), accompanied by phenocrysts and microphenocrysts of Fe–Ti oxides, and rare olivine (Fo_{69-49}) and orthopyroxene ($Wo_{5-3}En_{71-64}Fs_{33-25}$). Independent and small leucocratic domains are recognized within the framework built by coarser-grained plagioclase and clinopyroxene laths (Fig. 2a–b), and occur in all samples. In these isolated domains or pockets, microphenocrysts of predominantly quartz and alkali-feldspar ($An_{0.7-0.2}Ab_{23-13}Or_{86-76}$) are accompanied by biotite and apatite (Fig. 2c–h). Biotite and apatite occur as discrete crystals and have euhedral to subhedral shapes, whereas anhedral quartz and alkali-feldspar occupy the remaining space in these pockets, commonly displaying symplectic textures (i.e. quartz–feldspar intergrowths). Biotite does not occur as overgrowths or as reaction rims around primary minerals. This textural evidence (i.e. biotite appearing as discrete crystals with defined shapes) suggests that the biotites are of igneous origin. The more evolved assemblage of magmatic minerals with smaller crystal sizes in these pockets suggests that they represent evolved melts that crystallized subsequent to the main crystallization phase constituting the bulk of the dolerite, and they are hereinafter termed late-stage melt pockets. Representative mineral compositions for pyroxene, feldspar, olivine, and apatite are presented in Supplementary Tables S3–S6.

For 24 of the 26 analyzed samples, the degree of alteration is generally low, as reflected by loss on ignition (LOI) values generally below 3 wt.% (Table 1). In these samples, clinopyroxene and biotite are commonly partially altered to chlorite. Two samples (IBST-991 and IB-990) are however strongly altered, as reflected by LOI >6 wt.% (Table 1). In these samples, carbonate veins are present (Supplementary Fig. S1c), plagioclase has undergone incipient saussuritization, and clinopyroxene is almost completely altered to chlorite.

4.2. Whole-rock major elements

Whole-rock major element concentrations for the dolerites are presented in Table 1. All samples from the Solimões Basin and the majority of dolerites from the Amazonas Basin can be classified as low-Ti rocks, with TiO_2 concentrations <2.0 wt.%. Four samples (IBST-991, IB-990, MA-2883 and MA-2884) have TiO_2 concentrations ranging from 2.2 to 3.3 wt.%, and are therefore classified as high-Ti rocks. These four samples represent two different sills emplaced in lower Paleozoic clastic rocks in the eastern part of the Amazonas Basin (Fig. 1a–c). Note that two of these high-Ti samples (IBST-991 and IB-990) are strongly altered, with LOI >6 wt.% (Table 1; Supplementary Fig. S1). The low-Ti dolerites are basalts or basaltic andesites following the total alkali versus silica (TAS) classification diagram (compositions recalculated as anhydrous; Supplementary Fig. S2), with SiO_2 and Na_2O+K_2O concentrations ranging from 50 to 54 and 1.8 to 4.0 wt.%, respectively. The high-Ti samples have similar Na_2O+K_2O values (2.4 to 3.7 wt.%) but significantly lower SiO_2 concentrations (42 to 47 wt.%). The two unaltered high-Ti samples (MA-2883 and MA-2884) can be classified as basalts following the low-Ti dolerites. Except for the two altered high-Ti samples, the dolerites are quartz–hypersthene normative tholeiites.

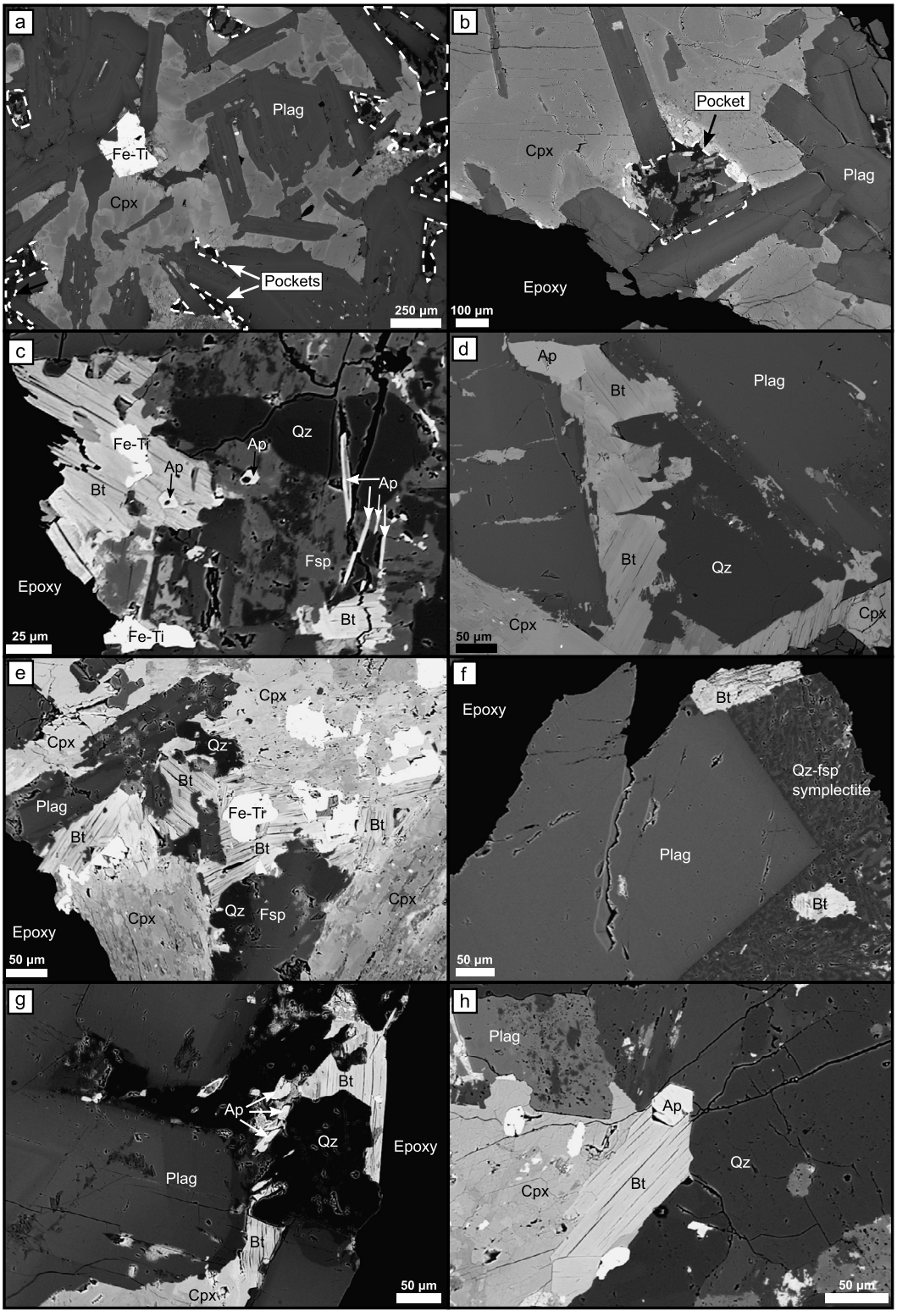

Fig. 2. Representative backscatter electron microprobe images of low- and high-Ti dolerites from the Amazonas and Solimões basins. The bulk of the dolerites are characterized by phenocrysts of clinopyroxene and plagioclase, accompanied by phenocrysts and microphenocrysts of Fe–Ti oxides, while independent pockets of microphenocrysts of quartz, alkali-feldspar, biotite and apatite occur within the framework of the bulk clinopyroxene and plagioclase (a)–(b). (c)–(h) Zoom-in of micropegmatitic pocket domains. (a) Sample OAST (low-Ti, Amazonas). (b) SOL-6 (low-Ti, Solimões Basin). (c) Sample SOL-1 (low-Ti, Solimões Basin). (d) Sample MA-2884 (high-Ti, Amazonas). (e) Sample MA-690/705 (low-Ti, Amazonas). (f) Sample ATZ-2106/2118 (low-Ti, Amazonas Basin). (g) Sample ATZ-2220-2247 (low-Ti, Amazonas Basin). (h) Sample SOL-7 (low-Ti, Solimões Basin). Fe–Ti = Fe–Ti oxide. Plag = plagioclase. Fsp = feldspar. Cpx = clinopyroxene. Bt = biotite. Ap = apatite. Qz = quartz.

The low- and unaltered high-Ti dolerites are relatively evolved, with Mg# (= 100 Mg/(Mg + Fe^{2+}), calculated for Fe^{3+}/Fe^{2+} = 0.15 following De Min et al., 2003) ranging from 48 to 65, and MgO concentrations varying between 5.3 and 7.8 wt.% (Table 1). In contrast, low-Ti samples SOL-6 and SOL-8 from the Solimões Basin trend towards a less evolved composition with Mg# and MgO of 69 to 70 and 7.9 to 9.6 wt.%, respectively. The highly altered high-Ti samples (IBST-991 and IB-990) have considerably lower Mg# (20 and 29) and MgO concentrations (<3 wt.%) compared to the total sample suite.

Considering the major elements, the studied dolerites plot within the range of previously analyzed high- and low-Ti CAMP sills and lavas in South America (Fig. 3; compositions recalculated as anhydrous). High-Ti CAMP rocks have generally lower SiO_2 and higher TiO_2, P_2O_5 and Fe_2O_3 whole-rock concentrations with respect to the low-Ti ones. For both high- and low-Ti CAMP rocks, SiO_2, Na_2O, K_2O and Fe_2O_3 decrease and CaO increases with increasing MgO, used as a differentiation index, whereas there is no apparent correlation for Al_2O_3. For high-Ti CAMP rocks, P_2O_5 and TiO_2 increase with decreasing MgO, whereas for low-Ti CAMP rocks these concentrations remain nearly constant.

4.3. Whole-rock trace elements

Whole-rock trace element concentrations for the dolerites are presented in Table 1 (and Supplementary Table S7). Primitive mantle normalized (McDonough and Sun, 1995) multielement diagrams are presented in Fig. 4a, showing a clear difference in incompatible trace element patterns for the low- and high-Ti dolerites. The low-Ti dolerites have generally negative anomalies for Nb, Ta, P, Ti and Y, and positive for Sr and K, whereas the high-Ti dolerites have negative anomalies for P, Y and K, and positive for Ta and Ti. The high-Ti dolerites have parallel trace element patterns, but overlap for Rb and K, and the altered high-Ti samples (IBST-991 and IB-990) are generally more enriched in incompatible elements, and especially in Ba. These compositions resemble those of the evolved high-Ti rocks described by Merle et al. (2011), but as alteration is very pronounced in these samples, this comparison will not be considered further. Notably, the crustal-like characteristics shown for the low-Ti Brazilian sills, such as depletion in high field strength elements (HFSE) and enrichment in large ion lithophile elements (LILE), is typical for low-Ti CAMP rocks (Marzoli et al., 2018). Likewise, the patterns shown by our high-Ti samples are similar to those generally observed for previously studied high-Ti CAMP rocks (e.g. De Min et al., 2003; Deckart et al., 2005; Merle et al., 2011).

C1-chondrite normalized (McDonough and Sun, 1995) REE diagrams (Fig. 4b) also show a clear difference between the low- and high-Ti dolerites. The Low-Ti sills show moderately sloping patterns with moderate values for Light REE on Heavy REE and Middle REE ratios (e.g. La/Yb_{CH} = 2.2 to 4.1 and La/Sm_{CH} = 1.3 to 2.2). In contrast, the high-Ti dolerites show slightly convex-upward patterns, with less fractionated LREE/HREE and LREE/MREE ratios (La/Yb_{CH} 2.5 to 2.9; La/Sm_{CH} = 1.2 to 1.9). MREE/HREE ratios overlap for the low- (Gd/Yb_{CH} = 1.4 to1.8) and high-Ti groups (Gd/Yb_{CH} = 1.5 to 1.9). As observed for the incompatible trace elements, the high-Ti dolerites all show parallel patterns, but the altered high-Ti samples (IBST-991 and IB-990) are more enriched in REE.

In agreement with the major element compositions, trace element concentrations demonstrate a more primitive character of samples SOL-6 and SOL-8 (low-Ti, Solimões Basin). This is reflected by lower incompatible trace element concentrations (Fig. 4a) and REE (Fig. 4b), and higher Cr (610 to 860 ppm) compared to the rest of the low-Ti group sills (Cr < 410 ppm) (Table 1).

4.4. Sr–Nd isotopes

The $^{143}Nd/^{144}Nd$ and $^{87}Sr/^{86}Sr$ isotope data for 24 dolerite samples are shown in Table 1. The isotopic ratios are back-calculated for radiogenic in-growth using the Sr and Rb trace element data for the samples (Table 1), and an age of 201 Ma based on U–Pb ages of the sills (Davies et al., 2017; Heimdal et al., 2018). The low- vs. high-Ti dolerites plot in different areas of the Sr–Nd isotopic space, overlapping with previously published Sr–Nd isotopic data for high- and low-Ti CAMP flows and intrusives (Marzoli et al., 2018; Fig. 5a). The low-Ti dolerites show a rather wide range in $^{143}Nd/^{144}Nd_{201Ma}$, between 0.51215 and 0.51244 (ε_{Nd} −4.54 to +1.15), and are negatively correlated with a large and radiogenic range of $^{87}Sr/^{86}Sr_{201Ma}$ (between 0.70568 and 0.70756), following the mantle–crust array. The high-Ti sills are characterized by higher $^{143}Nd/^{144}Nd_{201Ma}$ values compared to the low-Ti, ranging between 0.51260 and 0.51266 (ε_{Nd} +4.28 to +5.39). The unaltered high-Ti samples have low $^{87}Sr/^{86}Sr_{201Ma}$ values (0.70363 and 0.70397), which is typical for high-Ti CAMP rocks. Conversely, the two altered high-Ti samples display very high $^{87}Sr/^{86}Sr_{201Ma}$ values (0.70938 and 0.70988), which do not overlap with other high-Ti CAMP rocks (Fig. 5a). A comparison of these two samples with the evolved high-Ti CAMP group highlights the strong effect of alteration, reflected by the significantly higher $^{87}Sr/^{86}Sr_{201Ma}$ values in the samples studied here compared to the rocks analyzed by Merle et al. (2011) (~0.7035) at comparable $^{143}Nd/^{144}Nd_{201Ma}$.

4.5. Biotite compositions

Biotite compositions from 15 of the 26 studied dolerite samples are presented in Supplementary Tables S8–S12. Up to 20 individual biotite crystals were analyzed per sample (Table 2).

The majority of biotites are annitic in compositions, reflected by Fe# (atomic Fe/(Fe+Mg)) > 0.5 and Al^{IV} between 1.7 and 2.5 (Supplementary Fig. S3). Most samples are characterized by biotites with highly variable TiO_2 concentrations; the minimum TiO_2 concentration per sample varies between 0.0066 and 1.9 wt.% and the maximum varies between 3.1 and 5.4 wt.%. In contrast, sample SOL-6 (low-Ti, Solimões Basin) shows a more limited range where all biotite TiO_2 concentrations are above 3.2 wt.% (max. 5.0 wt.%). Based on TiO_2, FeO (+MnO) and MgO compositions, all biotites from sample SOL-6 classify as 'primary magmatic' (Supplementary Fig. S4).

The biotite Cl abundances are also highly variable, from below the detection limit (0.02 to 0.03 wt.%; Supplementary Table S13) up to 4.7 wt.%. The distribution of measured Cl, including maximum and average values per individual dolerite sample, is presented in Table 2. There is a clear relationship between biotite Cl concentrations and the lithology of the sill host-rock (Fig. 6a; Table 2). Dolerites that are emplaced in evaporite-bearing lithologies contain biotites with a wide range in Cl concentrations, whereas dolerites within clastic host-rock are characterized by biotites with a rather narrow range and low Cl concentrations (<1.0 wt.%). The former group includes all analyzed samples from borehole ATZ and sample MA-1490/1508 from the Amazonas Basin, as well as samples SOL-1, -4, -7 and -8 from the Solimões Basin (Fig. 1b–c). For these samples, the average (mean) Cl concentration per sample varies from 0.92 to 2.0 wt.%, and maximum Cl values range from 2.1 to 4.7 wt.% (Table 2). The latter group includes all analyzed high-Ti samples (MA-2883, MA-2884 and IB-990) and sample OAST from the Amazonas Basin (Fig. 1b), with an average Cl concentration per sample between 0.18 to 0.31 wt.% (Table 2). Sample SOL-6 from the Solimões Basin represents an exception, as this sample is emplaced in evaporite-bearing host-rock, yet comprises biotites with Cl concentrations <1.0 wt.% (Cl_{avg} = 0.44 wt.%).

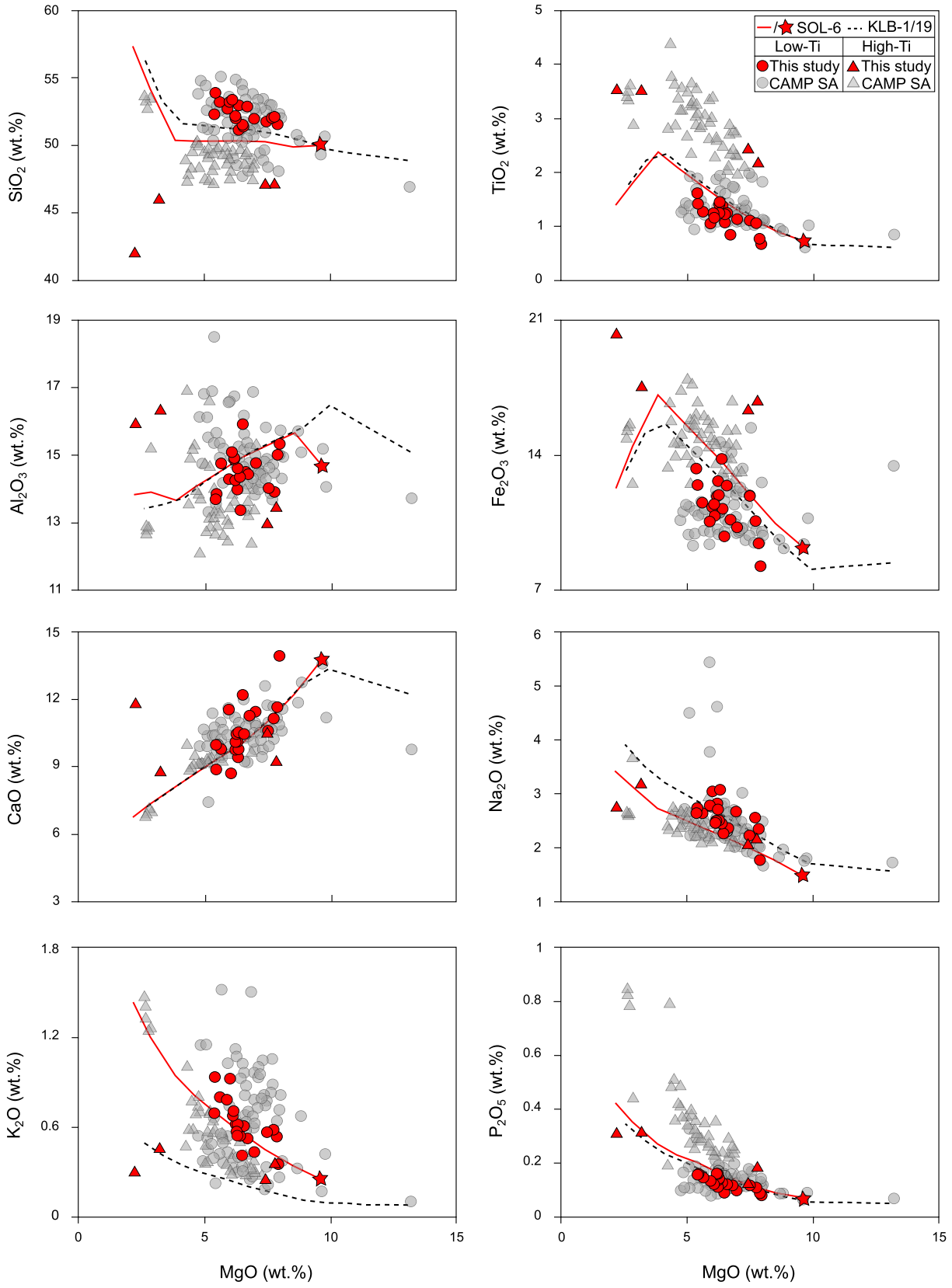

Fig. 3. Whole-rock major element diagrams for low- (circles) and high-Ti (triangles) CAMP rocks from South America show that low- and high-Ti dolerites from this study (red symbols) generally plot within the respective low- and high-Ti range of previously analyzed rocks from South America (grey symbols; Marzoli et al., 2018 and references therein). Black and red lines represent liquid lines of descent calculated with rhyolite-MELTS v.1.0.2 (Gualda et al., 2012) starting from dolerite sample SOL-6 from this study (red solid line) and a primitive tholeiitic melt obtained by experimental melting of a spinel peridotite at 15 kbar for ~20% partial melting (black dashed line; composition KLB-1 (run 19); Hirose and Kushiro, 1993). Fractional crystallization was modeled at 1 kbar for near-anhydrous compositions (0.2 wt.% H_2O in starting melt), with oxygen fugacity at the Quartz–Fayalite–Magnetite buffer. The low pressure is consistent with the basin history and shallow emplacement of the sills. The curves end at ~80% crystallization. Note that all major element compositions in these diagrams are recalculated as anhydrous.

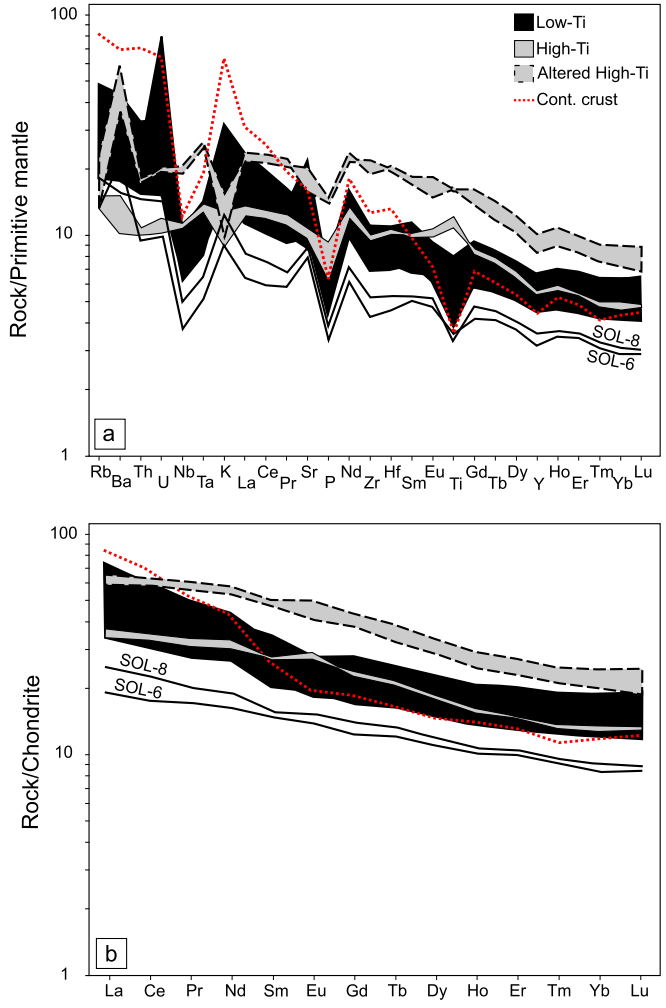

Fig. 4. (a) Primitive mantle normalized (McDonough and Sun, 1995) multielement diagrams for low- and high-Ti dolerites from this study. High-Ti dolerites (grey color) have negative anomalies for P, Y and K, and positive for Ta and Ti, whereas low-Ti dolerites (black color) have negative anomalies for Nb, Ta, P, Ti and Y, and positive for Sr and K, mimicking the trace element pattern of the continental crust (reported for comparison as red dotted line Kemp and Hawkesworth, 2004). Low-Ti samples SOL-6 and SOL-8 show depletion in incompatible elements compared to the remaining low-Ti dolerites. High-Ti samples IBST-991 and IB-990 (dashed lines) are generally more enriched in incompatible elements compared to the other low- and high-Ti dolerites. (b) C1-chondrite normalized (McDonough and Sun, 1995) Rare Earth Element (REE) diagrams for low- and high-Ti dolerites from this study. Low-Ti dolerites (black color) show moderately sloping patterns with Light REE on Heavy and Middle REE ratios of La/Yb_{CH} = 2.2 to 4.1 and La/Sm_{CH} = 1.3 to 2.2, respectively. Low-Ti samples SOL-6 and SOL-8 show depletion in REE compared to the remaining low-Ti dolerites. High-Ti dolerites (grey color) show slightly convex-upward patterns and lower LREE/HREE and LREE/MREE ratios (La/Yb_{CH} 2.5 to 2.9; La/Sm_{CH} = 1.2 to1.9). High-Ti samples IBST-991 and IB-990 (dashed lines) are more enriched in REE compared to the other low- and high-Ti dolerites.

Plots of Cl versus TiO_2 show two opposing trends (Supplementary Fig. S5; Fig. 6b). For samples with a narrow range and low Cl (<1.0 wt.%), Cl is positively correlated with TiO_2. For samples containing biotites with a wide range in Cl, an inverse relationship is observed, where Cl increases with decreasing TiO_2.

5. Discussion

5.1. Low- and high-Ti dolerites compared to CAMP globally

The geochemistry of the studied dolerites is remarkably uniform, considering the vast area of the Amazonas and Solimões basins ($> 1 \times 10^6$ km^2; Wanderley Filho et al., 2006), and is also consistent with that of previously studied CAMP rocks from the entire province. The CAMP is largely dominated by low-Ti basalts or basaltic andesites with depletion in HFSE and enrichment in LILE, and MgO concentrations between 4 and 10 wt.% (Marzoli et al., 2018), cropping out over all the areas covered by this LIP. High-Ti CAMP rocks are less common and are more localized than the low-Ti outcrops, being confined to areas close to the SE and NE margins of the West African and Amazonian cratons, respectively (Dupuy et al., 1988; De Min et al., 2003; Deckart et al., 2005; Merle et al., 2011; Klein et al., 2013; Marzoli et al., 2018). Most (22 out of 26) of the dolerites studied here are low-Ti rocks. The four high-Ti samples are from the eastern part of the Amazonas Basin (Fig. 1a–c), consistent with the spatial distribution of high-Ti rocks from previous studies in South America. The high-Ti dolerite from borehole MA is one of the westernmost occurrences of high-Ti CAMP rocks reported so far. It is worth noting that, based on the available chemical data, high-Ti dolerites are exclusively emplaced in the lower Paleozoic series, and they are represented in the deepest intercepted sills in both boreholes (Fig. 1b). Available samples from the Solimões Basin reveal only the presence of low-Ti dolerites, but it is unclear whether this is due to sampling bias, or an actual absence of high-Ti magmatism in this area.

In general, low-Ti CAMP rocks display relatively high $^{87}Sr/^{86}Sr_{201Ma}$ (0.7040 to 0.7080) coupled with moderately low $^{143}Nd/^{144}Nd_{201Ma}$ (0.5121 to 0.5125), while high-Ti rocks show more mantle-like Sr–Nd isotopic signatures ($^{87}Sr/^{86}Sr_{201Ma}$ 0.7030 to 0.7045; $^{143}Nd/^{144}Nd_{201Ma}$ 0.5125 to 0.5127; Marzoli et al., 2018; Fig. 5a). These features are also recognized in the low- and high-Ti samples studied here, with $^{87}Sr/^{86}Sr_{201Ma}$ between 0.70568 and 0.70756 for low-Ti dolerites, and 0.70363 and 0.70397 for unaltered high-Ti dolerites (Fig. 5a). Note that the anomalously high $^{87}Sr/^{86}Sr_{201Ma}$ values (0.70938 and 0.70988) observed for the high-Ti samples IBST-991 and IB-990 are likely a result of low temperature alteration, and should not be taken into account. The enriched isotopic character of low-Ti CAMP rocks is also apparent in Pb isotopes (Marzoli et al., 2018), which generally plot between enriched mantle pools (EMI and EMII; Zindler and Hart, 1986). These enriched Sr–Nd–Pb signatures, and other crustal-like geochemical characteristics such as depletion in HFSE and enrichment in LILE, coupled with mantle-like $^{187}Os/^{188}Os$ signatures (~0.13), are typical for low-Ti CAMP rocks. These have been repeatedly interpreted as inherited from an enriched mantle source rather than a result of crustal assimilation processes *en route* to the surface (see review in Marzoli et al., 2018).

Although the low-Ti dolerites studied here fall within the same Sr–Nd isotopic fields as previously analyzed low-Ti CAMP rocks, they generally show more radiogenic $^{87}Sr/^{86}Sr_{201Ma}$ values (at comparable $^{143}Nd/^{144}Nd_{201Ma}$ ratios) compared to lava flows and intrusive units from Brazil and elsewhere in South America (Fig. 5b). While the latter CAMP rocks generally plot within a range in $^{87}Sr/^{86}Sr_{201Ma}$ between 0.7043 and 0.7063, the majority of low-Ti dolerites from this study have $^{87}Sr/^{86}Sr_{201Ma}$ values >0.7063. These radiogenic $^{87}Sr/^{86}Sr_{201Ma}$ values could reflect an additional process, such as crustal contamination, exacerbating the already present enriched character, which is mantle-inherited and a typical feature of the entire low-Ti CAMP.

5.2. Chlorine in biotite as a tracer for evaporite-derived contamination of low-Ti magmas

Whole-rock $^{87}Sr/^{86}Sr_{201Ma}$ and Cl concentrations (mean per sample) in biotite are positively correlated (Fig. 5c), which suggests that the enrichment in $^{87}Sr/^{86}Sr_{201Ma}$ and Cl reflects the same geochemical process. There is a clear correlation between the Cl concentrations in biotite and host-rock lithology (Fig. 6a; Table 2), which strongly suggests that the Cl is evaporite-sourced.

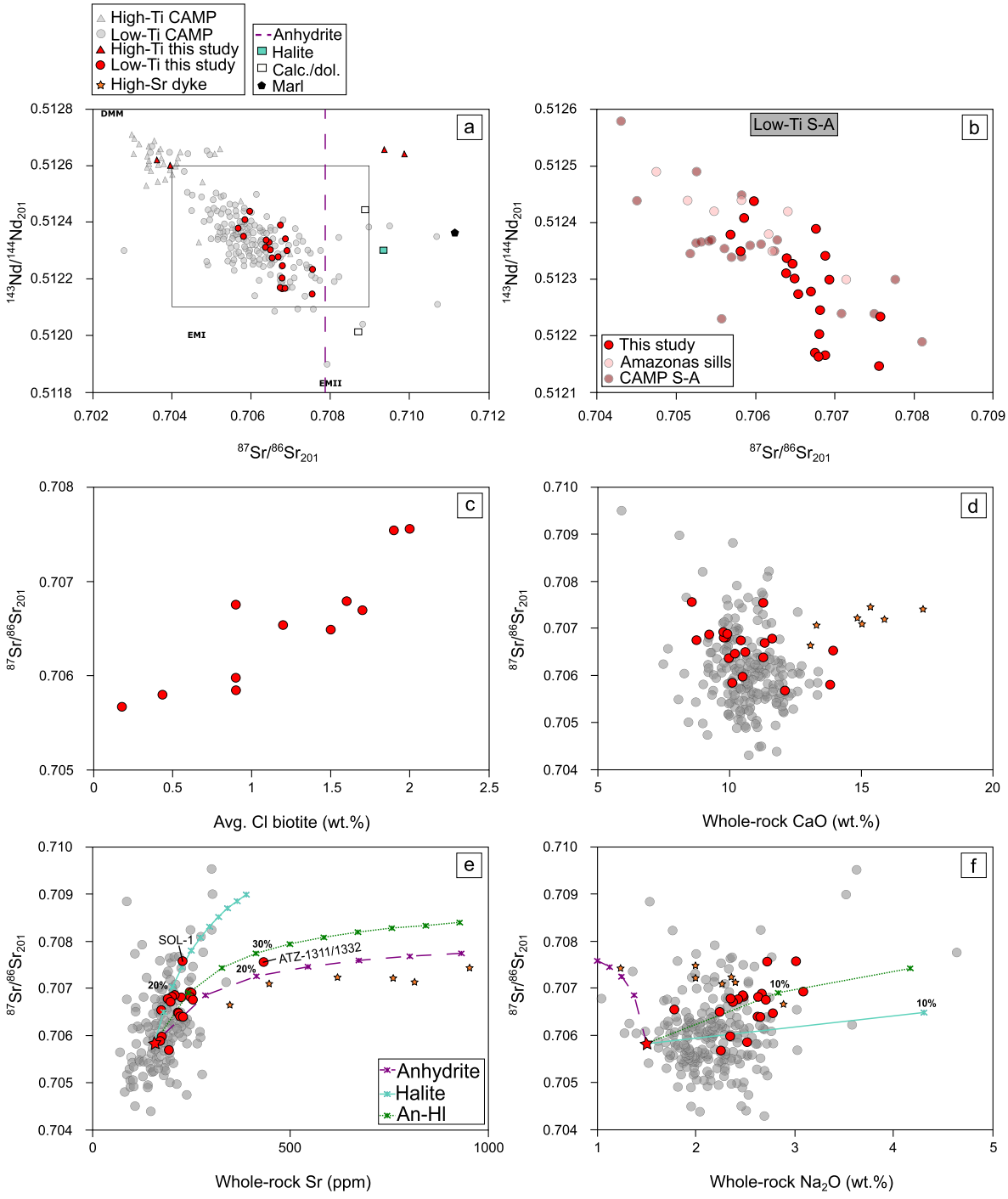

Fig. 5. (a) $^{87}Sr/^{86}Sr_{201Ma}$ and $^{143}Nd/^{144}Nd_{201Ma}$ compositions of low- (circles) and high-Ti (triangles) CAMP rocks from North America, South America, Africa, Europe, and Africa. Red symbols represent dolerites from this study, whereas grey symbols are from Marzoli et al. (2018) and references therein. Low-Ti CAMP rocks show a rather wide range in both $^{143}Nd/^{144}Nd_{201Ma}$ and $^{87}Sr/^{86}Sr_{201Ma}$ and follow the mantle–crust array, while high-Ti rocks are characterized by more homogeneous Sr–Nd isotopic compositions, with more radiogenic $^{143}Nd/^{144}Nd_{201Ma}$, but less radiogenic $^{87}Sr/^{86}Sr_{201Ma}$ values. The low- and high-Ti dolerites from this study plot within the respective low- and high-Ti range of CAMP globally. $^{87}Sr/^{86}Sr_{201Ma}$ and $^{143}Nd/^{144}Nd_{201Ma}$ compositions for depleted MORB mantle (DMM) and enriched mantle (EMI and EMII) are from Marzoli et al. (2018), and the various crustal rocks from Pang et al. (2013). Note that $^{143}Nd/^{144}Nd$ for anhydrite was not available, thus the $^{87}Sr/^{86}Sr_{201Ma}$ is shown as a vertical dashed line. The white square represents the Sr–Nd isotopic space shown in (b). (b) $^{87}Sr/^{86}Sr_{201Ma}$ versus $^{143}Nd/^{144}Nd_{201Ma}$ plots of low-Ti CAMP rocks from South America (zoom-in of (a)) show that the majority of samples fall within a range in $^{87}Sr/^{86}Sr_{201Ma}$ between 0.7043 and 0.7063, whereas the low-Ti dolerites studied here (red circles) have$^{87}Sr/^{86}Sr_{201Ma}$ values generally above 0.7063. Pink circles represent previously analyzed sills from the Amazonas Basin by De Min et al. (2003), whereas maroon circles represent extrusive and intrusive low-Ti rocks from the rest of South America (Marzoli et al., 2018 and references therein). (c)–(f) Plots of whole-rock $^{87}Sr/^{86}Sr_{201Ma}$ versus average (mean) chlorine content in biotite (per sample) and selected whole-rock major and trace elements for low-Ti dolerites studied here (red circles) show that Cl, Na_2O and Sr increase with increasing $^{87}Sr/^{86}Sr_{201Ma}$, whereas CaO decrease. Sample ATZ-1311/1332 (Amazonas Basin) is markedly enriched in Sr compared to the rest of the sample suite from this study (432 versus 147 to 254 ppm; Table 1), and follows high-Sr dykes from the Portuguese CAMP (Callegaro et al., 2014). Colored lines in (e) and (f) represent mixing models for potential contamination of the dolerites with anhydrite (purple dashed line; sample MD56-26), halite (light blue solid line; sample MD56-19), and an anhydrite/halite mix (An–Hl; green dotted line), starting from the composition of sample SOL-6 (red star). The anhydrite/halite mix represents a composition of 50% anhydrite (considering mean composition of samples MD56-22 and MD56-31) and 50% halite (sample MD56-19). Each symbol for each mixing curve represents 10% assimilation. $^{87}Sr/^{86}Sr_{201Ma}$ and Sr compositions for the various lithologies used in the mixing models are from Pang et al. (2013). Symbols follow the same legend as shown in (a). Calc./dol. = calcite/dolomite. S-A = South America.

Table 2
Distribution of measured chlorine concentrations in biotite from individual dolerite samples from the Amazonas and Solimões basins.

Sample	Depth (mbs)	Basin	TiO_2 content	Host rock	Crystal #	Analyses #	<1 (%)	1 to 2 (%)	2 to 3 (%)	3 to 4 (%)	4 to 5 (%)	Max. Cl (wt.%)	Avg. Cl
ATZ	1311–1332	AM	Low-Ti	E/L	9	12	17	42	17	25	0	3.7	1.9
ATZ	2106–2118	AM	Low-Ti	E/L	15	31	6	58	29	0	6.5	4.7	1.9
ATZ	2121–2130	AM	Low-Ti	E/L	19	35	60	26	11	3	0	3.3	0.92
ATZ	2200–2217	AM	Low-Ti	E/L	9	16	69	12	19	0	0	2.6	0.92
ATZ	2220–2247	AM	Low-Ti	E/L	18	42	57	38	5	0	0	2.1	0.93
MA	1490–1508	AM	Low-Ti	E/L	8	17	24	35	41	0	0	2.5	1.6
SOL-1	na	SO	Low-Ti	E/L	11	15	0	60	33	0	6.7	4.6	2.0
SOL-4	na	SO	Low-Ti	E/L	15	35	23	43	31	3	0	3.4	1.5
SOL-7	na	SO	Low-Ti	E/L	13	31	42	19	23	13	3.2	4.2	1.7
SOL-8	na	SO	Low-Ti	E/L	19	42	69	7	14	7	2.4	4.6	1.2
SOL-6	2888	SO	Low-Ti	E/L	11	15	100	0	0	0	0	0.87	0.44
OAST	382	AM	Low-Ti	C	20	36	100	0	0	0	0	0.89	0.18
MA	2883	AM	High-Ti	C	17	43	100	0	0	0	0	0.44	0.18
MA	2884	AM	High-Ti	C	13	33	100	0	0	0	0	0.64	0.31
IB	990	AM	High-Ti	C	10	14	100	0	0	0	0	0.60	0.21

mbs = meters below surface. na = not available. SO = Solimões Basin. AM = Amazonas Basin. Low-Ti = TiO_2 <2.0 wt.%. High-Ti = TiO_2 >2.0 wt.%. E/L = evaporite/limestone; layers of evaporite and limestone with varying relative abundance, interlayered with clastic rock, where evaporite and limestone are the dominant lithologies. C = clastic rock. Crystal # = number of analyzed biotite crystals for the individual dolerite sample. Analyses # = number of biotite analyses for the individual dolerite sample, including all biotite crystals. Max. Cl = maximum biotite chlorine value for the individual dolerite sample, including all biotite crystals. Avg. Cl = average (mean) biotite chlorine value for the individual dolerite sample.

Biotites from sills emplaced in clastic rocks have Cl concentrations <0.9 wt.% (mean Cl concentration per sample between 0.18 and 0.31 wt.%.; Table 2), which is within the common range for biotite (<1.0 wt.%; Léger et al., 1996). Similar Cl concentrations are reported for biotites from mafic/ultramafic intrusives, such as the Stillwater Complex (up to 0.41 wt.%; Boudreau et al., 1997), Bushveld Complex (up to 0.93 wt.%; Willmore et al., 2000), Skaergaard intrusion (up to 0.28 wt.%; Nash, 1976), Mont Saint-Hilaire complex (up to 0.13 wt.%; Teiber et al., 2015) and Lofoten Islands (up to 0.2 wt.%; Teiber et al., 2015). In contrast, dolerites emplaced in evaporite-bearing host-rock contain extremely Cl-enriched biotites (Cl_{max} = 2.1 to 4.7 wt.%; Table 2), which are comparable to those found in skarns (up to 7.15 wt.%; Tracy, 1991) or granulite-facies gneiss (up to 4.64 wt.%; Léger et al., 1996). Note that there also appears to be a correlation between host-rock lithology and Cl concentrations in apatite (Supplementary Table S6), but the small dataset ($n = 22$) limits the possibility of further interpretation.

Sample SOL-6, which is also emplaced in evaporite-bearing host-rock (Fig. 1c), shows a much weaker crustal imprint, with Cl concentrations in biotite <0.1 wt.% (Table 2) and whole rock $^{87}Sr/^{86}Sr_{201Ma}$ of 0.7058 (Table 1). This sample displays the most primitive features of the entire sample suite, reflected by higher whole-rock MgO and Cr, and lower whole-rock SiO_2 and incompatible element concentrations, compared to the other dolerites. As seen in Fig. 3, the low-Ti dolerites generally follow the liquid line of descent for fractional crystallization (calculated with MELTS) with sample SOL-6 as the starting composition, suggesting that the low-Ti dolerites crystallized during closed-system evolution of a melt similar in composition of SOL-6. However, the elevated biotite Cl concentrations in the same low-Ti samples clearly point toward an open-system evolution. Plots of whole-rock major and trace elements versus $^{87}Sr/^{86}Sr_{201Ma}$ and Cl concentrations (mean per sample) in biotite, generally display positive correlations for whole-rock SiO_2, Na_2O, K_2O and LILEs, and negative correlations for MgO and CaO (Fig. 5c–f, Fig. 7). These trends suggest that along with magmatic evolution (most likely by fractional crystallization), contamination occurred by means of a Cl-rich agent. Biotites from sample SOL-6 have high TiO_2 concentrations, and classify as primary magmatic phases according to the diagram shown in Supplementary Fig. S4. Therefore, biotite compositions in sample SOL-6 likely reflect the magma composition prior to evaporite contamination.

The Ti content in biotite is dependent on temperature; the solubility of Ti in biotite generally decreases with decreasing temperature with respect to magmas (Robert, 1976). Plots of TiO_2 versus Cl concentrations in the studied biotites show two opposing trends (Fig. 6b; Supplementary Fig. S5). For biotites from sample SOL-6 and sills emplaced in clastic host-rock (OAST, IB-990 and MA-2883/2884), Cl and TiO_2 concentrations in biotite are generally positively correlated. This likely reflects a Cl degassing trend during cooling and crystallization of a non-contaminated magma (Fig. 6b). For biotites with Cl concentrations >1.0 wt%, Cl generally increases with decreasing TiO_2 (Fig. 6b). This is interpreted to follow an input of Cl into the magmatic system during crystallization of the dolerites, where the Cl is evaporite-sourced. Notably, the Cl solubility in biotite increases with decreasing water activity in pore fluids (e.g. Svensen et al., 2001). If pore fluids (e.g. brines) were involved during the contamination process, the observed increase in Cl with decreasing TiO_2 could reflect crystallization of biotites during interaction with an increasingly saline brine during cooling.

5.3. Mechanisms for evaporite-derived contamination

Possible mechanisms for evaporite-derived contamination of magmas include diffusive transfer of elements via brines, chemical dissolution of evaporite, or partial melting of evaporite within the magma (Ripley et al., 2003; Li et al., 2009; Pang et al., 2013; Schofield et al., 2014; Iacono-Marziano et al., 2017; Yudovskaya et al., 2018). Laboratory experiments have shown that basaltic magmas (at 1250 °C) can dissolve up to 4.7 wt.% Cl at crustal depths (2 kbar) in the presence of Cl-bearing fluids (Chevychelov and Suk, 2003). Most studies favor contamination by fluids as opposed to evaporite melting, but these studies consider only anhydrite, which has a very high melting point (~1450 °C). Halite has a much lower melting point (~800 °C), and evaporites of mixed mineralogical compositions are likely to have substantially lower solidus temperatures (Pang et al., 2013; Yudovskaya et al., 2018). For example, melting textures of salts in contact with thin (tens of cm to 5 m) basaltic Miocene dykes in Germany have been reported (Schofield et al., 2014), and elevated $^{87}Sr/^{86}Sr$ values in these dykes have been interpreted to reflect assimilation of the salts (Steinmann et al., 1999). Notably, the evaporite deposits in the Amazonas and Solimões basins consist of lithologies showing varying relative

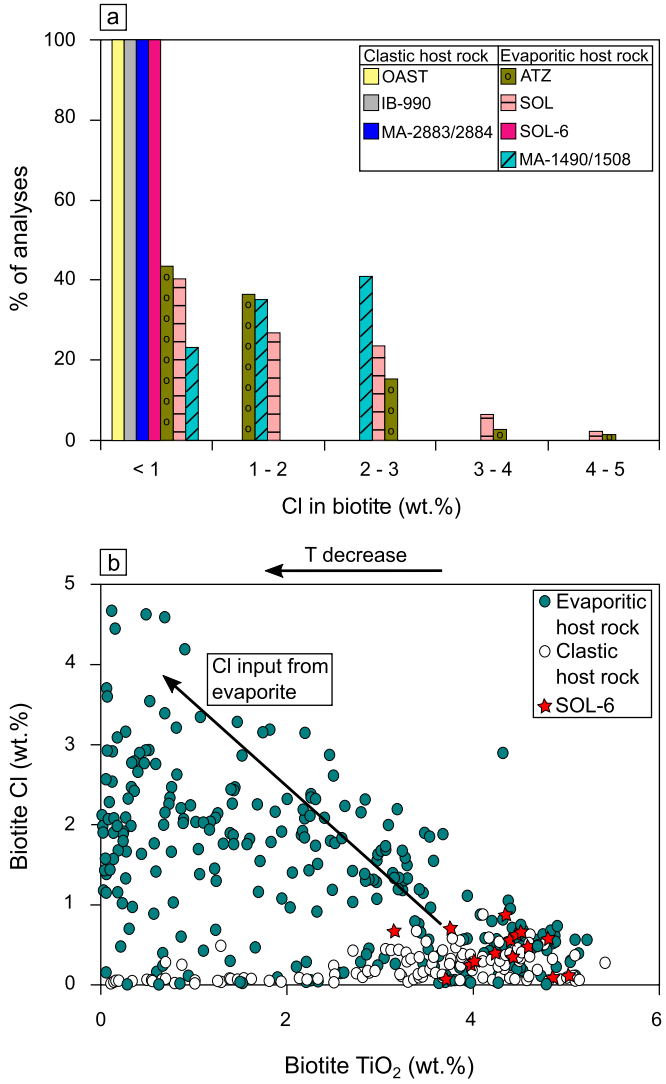

Fig. 6. (a) There is a clear correlation between host-rock lithology and Cl concentrations in the analyzed biotites. Biotite from sills emplaced in clastic host-rock have Cl concentrations <1.0 wt.%, whereas biotites from sills emplaced in evaporitic host-rock show a wide range in Cl. Columns OAST, IB-990, SOL-6 and MA-1490/1508 represent biotite analyses from individual dolerite samples, whereas columns SOL and ATZ include biotite measurements from several sills from the respective boreholes (see Table 2). Note that MA-2883/2884 includes biotite analyses from two individual samples from the same sill. (b) The positive correlation between Cl and TiO_2 biotite concentrations observed for sills emplaced in clastic host-rock (OAST, IB-990 and MA-2883/2884; white circles) is interpreted to represent a Cl degassing trend during cooling and crystallization of a non-contaminated magma, here represented by sample SOL-6 (red stars). In contrast, the increase in Cl with decreasing TiO_2 observed for sills emplaced in evaporitic host-rock (ATZ, SOL and MA-1490/1508; green circles) is interpreted to represent an input of Cl into the magmatic system during the crystallization of the dolerites. Note that this figure represents a compilation of all plots shown in Supplementary Fig. S5.

abundances of halite and anhydrite, which are interlayered with limestone and clastic rocks (Supplementary Fig. S6).

The high Cl concentrations in magmatic biotites from the dolerites likely reflect halite contamination. Anhydrite contamination would enrich the magmas in Ca and S (Iacono-Marziano et al., 2017). Sulfur was not analyzed in the studied dolerites, and there is no evidence for the rocks studied here being enriched in Ca compared to previously analyzed CAMP rocks (Fig. 3, Fig. 5d). The whole-rock Ca concentrations seem to be controlled only by fractional crystallization or accumulation of Ca-bearing minerals (e.g. augite or plagioclase). One sample (ATZ-1311/1332; Amazonas Basin; Supplementary Fig. S6) is, however, significantly enriched in Sr (432 ppm) compared to the rest of the sample suite (up to 254 ppm; Table 1, Fig. 5e). The Sr concentration in this sample is similar to high-Sr dykes from the Portuguese CAMP (348 to 1046 ppm), rocks that are suggested to reflect up to 20% assimilation of carbonate (Callegaro et al., 2014). This sample and sample SOL-1 have markedly higher $^{87}Sr/^{86}Sr_{201Ma}$ values (0.7075 and 0.7076) compared to the rest of the sample suite, but sample SOL-1 has ~50% less Sr (227 vs. 432 ppm; Table 1, Fig. 5e). Host-rocks that are present in the Amazonas and Solimões basins (i.e. anhydrite, halite, marl, and limestone) have generally similar $^{87}Sr/^{86}Sr$ values (~0.708 for anhydrite and 0.709 to 0.710 for halite, marl and limestone), but anhydrite is significantly enriched in Sr (540 to 1829 ppm) compared to the other lithologies (<600 ppm; Dean, 1987 and references therein; Rodrigues et al., 1997; Neto, 2010; Da Silva, 2012; Pang et al., 2013).

We calculated a series of simple mixing curves (Fig. 5e–f) between sample SOL-6, representing uncontaminated magma, and potential contaminants, represented by Devonian evaporites from the Tunguska Basin (Pang et al., 2013). The $^{87}Sr/^{86}Sr_{201Ma}$ and Sr content of sample ATZ-1311/1332 (high-Sr dolerite) is best explained by 20 to 30% addition of an anhydrite-dominated evaporite (with Sr between ~1000 and 1500 ppm), while the composition of sample SOL-1 is simulated via ~30% addition of a contaminant with a Sr concentration equivalent to halite (~400 ppm Sr). The remaining samples reflect generally <15% addition of a contaminant with varying halite and anhydrite abundances, which is also shown by plots of whole-rock Na_2O versus $^{87}Sr/^{86}Sr_{201Ma}$ (Fig. 5f). As previously mentioned, the dolerites are not markedly enriched in whole-rock Ca or Na, which would likely be expected with substantial evaporite assimilation. Also, since the actual mechanism of evaporite incorporation is not known, simple mixing might not quantify evaporite assimilation correctly, and these mixing lines should be considered only qualitative. In summary, the strongest geochemical evidence for contamination is the high Cl concentration in biotite, and based on the data presented here the main contaminant seems to be halite-dominated.

The mechanism of Cl incorporation into the sills remains speculative. It could have occurred through partial melting or chemical dissolution of evaporite, via brines, or by a combination of the different processes. However, as high-Cl biotites are only found within the late-stage pocket domains, and because the textural evidence suggests that the biotites are of igneous origin, we can argue that the mechanism(s) occurred while the dolerites were still crystallizing. During sill cooling, a solid crystal network with interstitial melt will form at a certain stage (Marsh, 1988, 1996; Philpotts and Carroll, 1996). With further cooling, the interstitial crystallizing melt will increase its density, but the strong crystal network effectively behaves as a solid and resists a volume change of the sill, generating a large underpressure (Svensen et al., 2010). Fluids, partial melts or even mobilized sediments (Aarnes et al., 2008; Svensen et al., 2010) can follow this negative pressure gradient and move from the country rocks towards the sill. This may explain why the evaporite-contamination of the dolerites seems to be restricted to the interstitial domains that we describe as evolved late-stage melt pockets.

5.4. Fate of volatiles and implications for the end-Triassic extinction

The emplacement of a subvolcanic LIP complex in a sedimentary basin can lead to substantial volatile release, taking both magmatic and contact metamorphic processes into account (Fig. 8). Assimilation of volatile rich host-rocks or fluids would add sediment-derived volatiles to the magma, increasing the total magma volatile content (adding to the already present mantle-derived volatiles). Contact metamorphism of the host-rocks would also generate

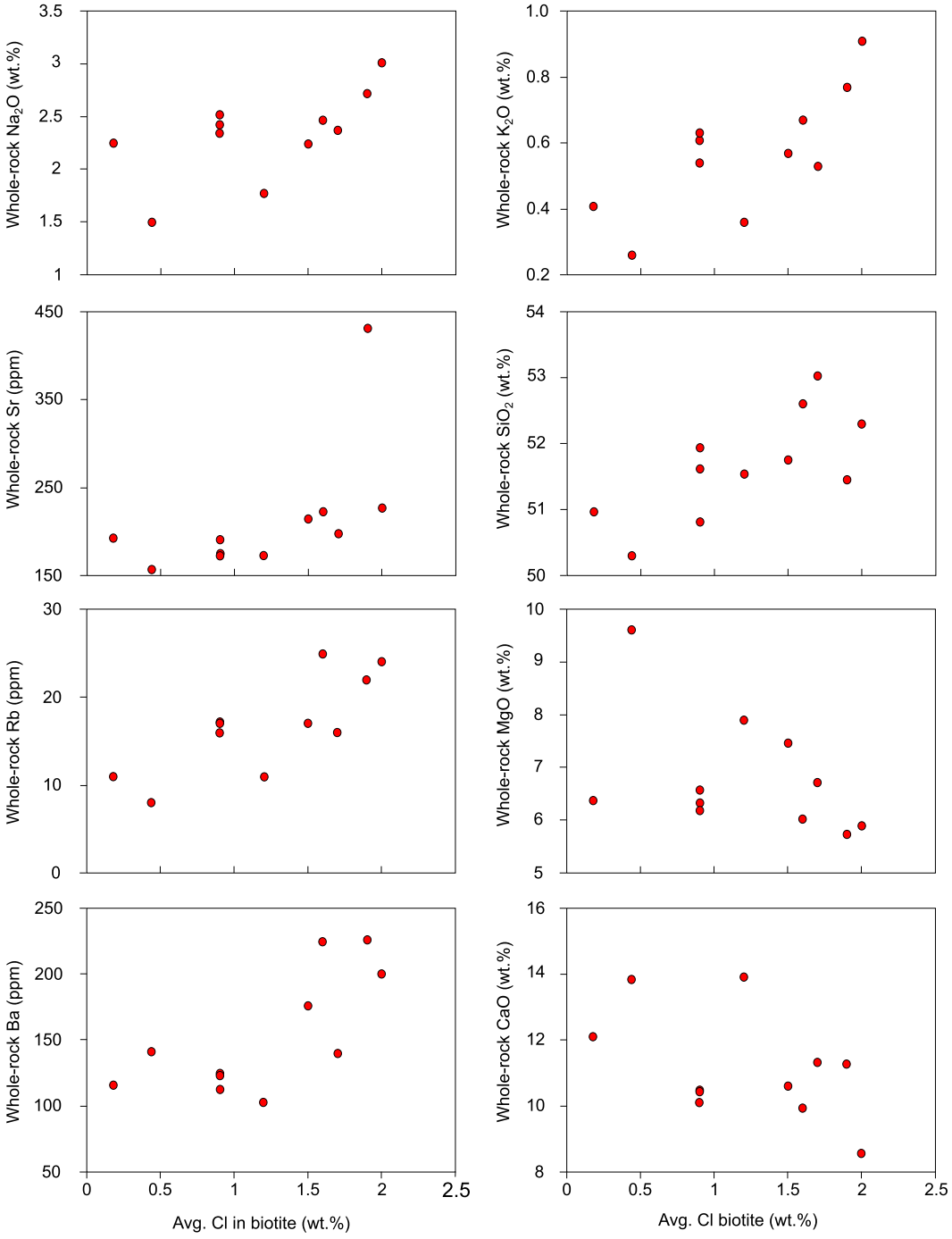

Fig. 7. Plots of whole-rock major and trace elements versus the average (mean) chlorine (Cl) concentration in biotite per sample for low-Ti dolerites from the Amazonas and Solimões basins show that SiO_2, Na_2O, K_2O, Sr, Rb and Ba generally increase with increasing Cl, whereas MgO and CaO decrease. These trends suggest that contamination occurred (by means of a Cl-rich agent) along with the magmatic evolution. The two different trends observed for Cl versus MgO and Na_2O represent samples from the Amazonas versus the Solimões basins.

sediment-derived volatiles, which would be in addition to the volatiles present in the magma. CH_4 and/or CO_2 would be generated from interactions between magma and organic-rich shale and coal, CO_2 from limestone, and SO_2 and/or halogens (e.g. HCl) from evaporites (Svensen et al., 2004, 2009; Iacono-Marziano et al., 2017; Ganino and Arndt, 2009; Sobolev et al., 2009; Aarnes et al., 2011; Pang et al., 2013; Black et al., 2012). If organic matter or petroleum is present in evaporites, CH_4 and halocarbons (e.g. CH_3Cl, CH_3Br) may also form (Svensen et al., 2009; Aarnes et al., 2011).

Volatiles are released from lavas during eruptions, from intrusives at crustal levels through fractures and/or high permeability zones in the basins, and/or through explosion pipes/hydrothermal vents (Fig. 8). Explosive pipes/vents and craters associated with sill emplacement and sedimentary degassing of several other LIPs are recognized in the Vøre, Møre, Karoo and Tunguska basins (e.g. Svensen et al., 2004, 2009), but these features have not yet been documented in the Amazonas and Solimões basins.

Recent modeling has shown that up to 88,000 Gt CO_2 could have been generated from contact metamorphism of limestone and

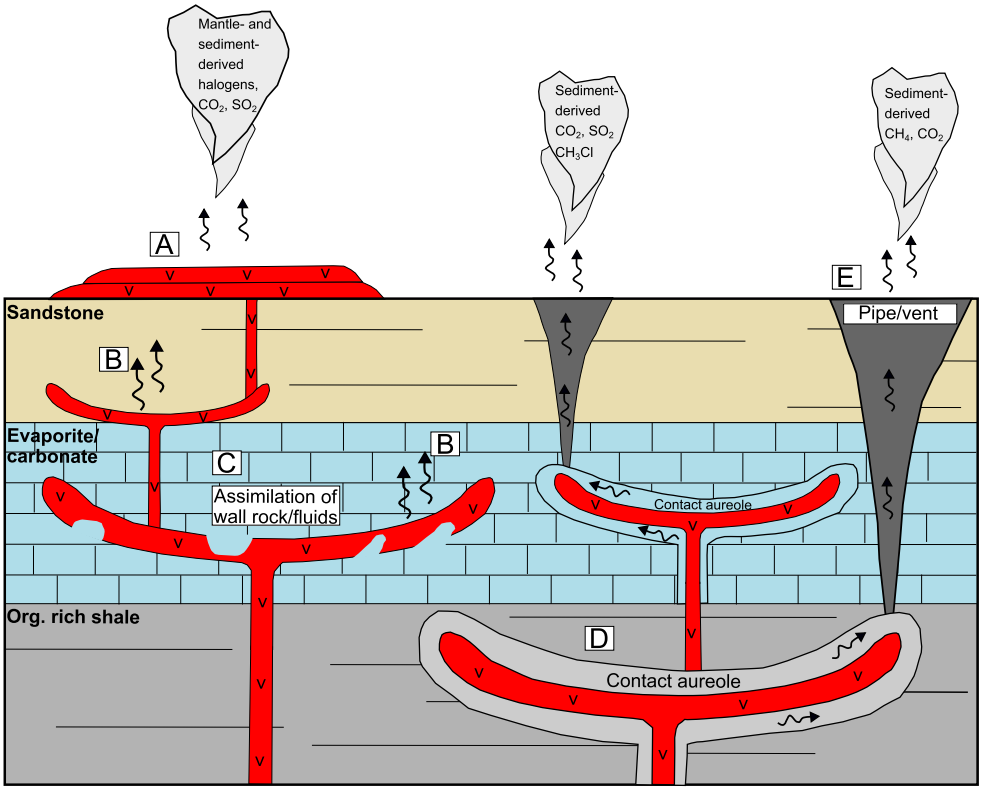

Fig. 8. Schematic cross-section of a volcanic basin illustrating the potential magmatic- and metamorphic processes generating and/or releasing mantle- and sediment-derived volatiles during the emplacement of a Large Igneous Province. (A) Release of mantle- and sediment-derived volatiles from the magma during eruption. (B) Decompression and/or crystallization-induced degassing of volatiles from the magma can occur prior to eruption. These gases can escape to the atmosphere through fractures and/or high permeability rocks in the basin. (C) Assimilation of volatile-rich wall rock (or volatile-rich fluids) increases the volatile concentration of the magma. (D) Heating and contact metamorphism of wall rock generates thermogenic gases. (E) Thermogenic gases are released to the atmosphere through explosion vents/pipes along sill edges that form due to rapid gas generation and pressure build-up. Note that the cross-section is not drawn to scale.

organic-rich shale in the Amazonas and Solimões basins (Heimdal et al., 2018), with a likely global warming effect if released to the atmosphere. Our data do not allow for quantification of the total amount of incorporated Cl in the magmas, and do not constrain the ratio of degassed versus biotite-bound Cl. Still, it is evident that magma–evaporite interactions led to an increase of the Cl content of the low-Ti magmas. Radiogenic $^{87}Sr/^{86}Sr_{201Ma}$ values (up to 0.7076) and Cl-rich biotites (up to 4.7 wt.%) observed in dolerites from both the Amazonas and Solimões basins (area $>1 \times 10^6$ km^2; Wanderley Filho et al., 2006), suggest that the process occurred on a large scale. This large-scale evaporite contamination of the sub-volcanic complex potentially led to the release of significantly more Cl, as opposed to release of mantle-derived Cl only. This could have had major implications for the end-Triassic environment through atmospheric poisoning and ozone depletion (Svensen et al., 2009; Aarnes et al., 2011; Black et al., 2012). High precision zircon U–Pb dating demonstrates synchrony between the low-Ti CAMP dolerites and the ETE (Davies et al., 2017; Heimdal et al., 2018), thus sill emplacement in the Amazonas and Solimões basins appears to have both a causal and temporal link to the ETE.

6. Conclusions

We report the presence and geochemistry of widespread low-Ti and minor high-Ti CAMP sills emplaced in the Amazonas and Solimões basins in Brazil. Radiogenic whole-rock $^{87}Sr/^{86}Sr_{201Ma}$ values and high Cl concentrations in magmatic biotites crystallized from sills present in an area over 1×10^6 km^2 are evidence for large-scale crustal contamination of the low-Ti magmas. The clear correlation between Cl content in biotite and host-rock lithology strongly implies that the Cl is evaporite-sourced. The incorporation of Cl in the dolerites could have occurred by partial melting or chemical dissolution of halite-rich evaporite, by brine assimilation, or a combination of the different processes. The contamination may have had major implications for the CAMP volatile budget, and likely increased the release of toxic and ozone-depleting Cl-compounds. Our findings support the hypothesis of a causal link between CAMP and the end-Triassic crisis, where the sills in the Brazilian basins played a key role in the volatile release through sill-sediment interactions. This strengthens the case for an active involvement of the sub-volcanic parts of LIPs in driving climate change and mass extinctions.

Acknowledgements

We wish to thank the Agência Nacional do Petróleo, Gás Natural e Biocombustíveis (ANP) and the HRT Brazilian Oil Company for providing dolerite samples and borehole logs. THH, SC, HHS, MTJ, and SP are supported by the Research Council of Norway through its Centres of Excellence funding scheme, project number 223272, and EP by CNPq (grant number 306.777/2017-7) and FAPERJ (grant number 202.854/2018). MTJ is also supported by the Research Council of Norway, project number 263000. Yuval Ronen is thanked for performing the Sr and Nd isotopic analyses. Muriel Erambert is thanked for assistance with the electron microprobe analyses. Else Ragnhild Neumann is thanked for her participation in discussions regarding the manuscript. We also wish to thank reviewers Andrea Marzoli and Giada Iacono-Marziano and Editor Derek Vance, whose contributions greatly improved the manuscript.

Appendix A. Supplementary material

Supplementary material related to this article can be found online at https://doi.org/10.1016/j.epsl.2018.11.018.

References

Aarnes, I., Podladchikov, Y., Neumann, E.R., 2008. Post-emplacement melt flow induced by thermal stresses: implications for differentiation in sills. Earth Planet. Sci. Lett. 276, 152–166.

Aarnes, I., Fristad, K., Planke, S., Svensen, H., 2011. The impact of host-rock composition on devolatilization of sedimentary rocks during contact metamorphism around mafic sheet intrusions. Geochem. Geophys. Geosyst. 12 (10).

Alves, D.B., Rodrigues, R., 1985. Influência das intrusões ígneas nos folhelhos devonianos da bacia do Baixo Amazonas. Rev. Bras. Geoci. 15 (2), 110–115.

Black, B.A., Elkins-Tanton, L.T., Rowe, M.C., Peate, I.U., 2012. Magnitude and consequences of volatile release from the Siberian traps. Earth Planet. Sci. Lett. 317, 363–373.

Blackburn, T.J., et al., 2013. Zircon U–Pb geochronology links the end-Triassic extinction with the Central Atlantic Magmatic Province. Science 340 (6135), 941–945.

Bond, D.P.G., Wignall, P.B., 2014. Large igneous provinces and mass extinctions: an update. Spec. Pap., Geol. Soc. Am. 505.

Boudreau, A.E., Stewart, M.A., Spivack, A.J., 1997. Stable Cl isotopes and origin of high-Cl magmas of the Stillwater Complex, Montana. Geology 25 (9), 791–794.

Callegaro, S., et al., 2014. Enriched mantle source for the Central Atlantic magmatic province: new supporting evidence from southwestern Europe. Lithos 188, 15–32.

Chevychelov, V.Yu., Suk, N.I., 2003. Influence of the composition of magmatic melt on the solubility of metal chlorides at pressures of 0.1–3.0 kbar. Petrology 11, 62–74.

Coombs, M.L., Sisson, T.W., Kimura, J.-I., 2004. Ultra-high chlorine in submarine Kilauea glasses: evidence for direct assimilation of brine by magma. Earth Planet. Sci. Lett. 217, 297–313.

Da Silva, M., 2012. Estudo Paleoambiental dos Carbonatos Pensilvanianos da Borda Norte da Bacia do Amazonas – Região do Rio Jatapú. Master Thesis. Universidade Federal do Amazonas.

Davies, J.H.F.L., et al., 2017. End-Triassic mass extinction started by intrusive CAMP activity. Nat. Commun. 8, 15596.

De Min, A., et al., 2003. The Central Atlantic Magmatic Province (CAMP) in Brazil: petrology geochemistry, $^{40}Ar/^{39}Ar$ ages, paleomagnetism and geodynamic implications. In: Hames, W.E., McHone, J.G., Munha, J. (Eds.), The Central Atlantic Magmatic Province: Insights from Fragments of Pangea. In: AGU Geophysical Monographs, pp. 91–128.

Dean, W.E., 1987. Trace and minor elements in evaporites in Marine evaporites. In: Dean, W.W., Schreiber, C.C. (Eds.), Marine Evaporites. The Society of Economic Paleontologists and Mineralogists, pp. 86–104.

Deckart, K., Bertrand, H., Liégeois, J.P., 2005. Geochemistry and Sr, Nd, Pb isotopic composition of the Central Atlantic Magmatic Province (CAMP) in Guyana and Guinea. Lithos 82 (3), 289–314.

Dupuy, C., Marsh, J., Dostal, J., Michard, A., Testa, S., 1988. Asthenospheric and lithospheric sources for Mesozoic dolerites from Liberia (Africa): trace element and isotopic evidence. Earth Planet. Sci. Lett. 87, 100–110.

Ganino, C., Arndt, N.T., 2009. Climate changes caused by degassing of sediments during the emplacement of large igneous provinces. Geology 37 (4), 323–326.

Gonzaga, F.G., Gonçalves, F.T.T., Coutinho, L.F.C., 2000. Petroleum geology of the Amazonas Basin, Brazil: modeling of hydrocarbon generation and migration. In: Mello, M.R., Katz, B.J. (Eds.), Petroleum Systems of South Atlantic Margins. In: AAPG Memoir, pp. 159–178.

Gualda, G.A.R., Ghiorso, M.S., Lemons, R.V., Carley, T.L., 2012. Rhyolite-MELTS: a modified calibration of MELTS optimized for silica-rich, fluid-bearing magmatic systems. J. Petrol. 53, 875–890.

Heimdal, T.H., et al., 2018. Large-scale sill emplacement in Brazil as a trigger for the end-Triassic crisis. Sci. Rep. 8, 141.

Hirose, K., Kushiro, I., 1993. Partial melting of dry peridotites at high pressures: determination of compositions of melts segregated from peridotite using aggregates of diamond. Earth Planet. Sci. Lett. 114, 477–489.

Iacono-Marziano, G., Ferraina, C., Gaillard, F., Di Carlo, I., Arndt, N.T., 2017. Assimilation of sulfate and carbonaceous rocks: experimental study, thermodynamic modeling and application to the Noril'sk–Talnakh region (Russia). Ore Geol. Rev. 90, 399–413.

Jones, M.T., Jerram, D.A., Svensen, H.H., Grove, C., 2016. The effects of large igneous provinces on the global carbon and sulphur cycles. Palaeogeogr. Palaeoclimatol. Palaeoecol. 441, 4–21.

Kemp, A.I.S., Hawkesworth, C.J., 2004. Granitic perspectives on the generation and secular evolution of the continental crust. In: Holland, H.D., Turekian, K.K. (Eds.), Treatise on Geochemistry, vol. 3. Elsevier, pp. 349–410.

Klein, E.L., Angélica, R.S., Harris, C., Jourdan, F., Babinski, M., 2013. Mafic dykes intrusive into Pre-Cambrian rocks of the São Luís cratonic fragment and Gurupi Belt (Parnaíba Province), north-northeastern Brazil: geochemistry, Sr–Nd–Pb–O isotopes, $^{40}Ar/^{39}Ar$ geochronology, and relationships to CAMP magmatism. Lithos 172–173, 222–242.

Léger, A., Rebbert, C., Webster, J., 1996. Cl-rich biotite and amphibole from Black Rock Forest, Cornwall, New York. Am. Mineral. 81, 495–504.

Li, C., Ripley, E.M., Naldrett, A.J., Schmitt, A.K., Moore, C.H., 2009. Magmatic anhydrite–sulfide assemblages in the plumbing system of the Siberian Traps. Geology 37 (3), 259–262.

Lindström, S., et al., 2017. A new correlation of Triassic–Jurassic boundary successions in NW Europe, Nevada and Peru, and the Central Atlantic Magmatic Province: a time-line for the end-Triassic mass extinction. Palaeogeogr. Palaeoclimatol. Palaeoecol. 478, 80–102.

Marsh, B.D., 1988. Crystal capture, sorting, and retention in convecting magma. Geol. Soc. Am. Bull. 100, 1720–1737.

Marsh, B.D., 1996. Solidification fronts and magmatic evolution. Mineral. Mag. 60, 5–40.

Marzoli, A., et al., 1999. Extensive 200-million-year-old continental flood basalts of the Central Atlantic Magmatic Province. Science 284 (5414), 616–618.

Marzoli, A., et al., 2018. The Central Atlantic Magmatic Province (CAMP): a review. In: Tanner, L. (Ed.), The Late Triassic World: Earth in a Time of Transition. Springer, pp. 91–125.

McDonough, W.F., Sun, S.S., 1995. The composition of the Earth. Chem. Geol. 120, 223–254.

Merle, R., et al., 2011. $^{40}Ar/^{39}Ar$ ages and Sr–Nd–Pb–Os geochemistry of CAMP tholeiites from Western Maranhão basin (NE Brazil). Lithos 122 (3), 137–151.

Michael, P.J., Schilling, J-G., 1989. Chlorine in mid-ocean ridge magmas: evidence for assimilation of seawater-influences components. Geochim. Cosmochim. Acta 53, 3131–3143.

Milani, E.J., Zalán, P.V., 1999. An outline of the geology and petroleum systems of the Paleozoic interior basins of South America. Episodes 22, 199–205.

Nash, W.P., 1976. Fluorine, chlorine and OH-bearing minerals in the Skaergaard intrusion. Am. J. Sci. 276, 546–557.

Neto, J.M., 2010. Geologia Isotópica (Sr, C e O) de Carbonatos da Formação Itaituba, Borda sul da Bacia do Amazonas. Master Thesis. Universidade Federal do Pará.

Pang, K.N., et al., 2013. A petrologic, geochemical and Sr–Nd isotopic study on contact metamorphism and degassing of Devonian evaporites in the Norilsk aureoles, Siberia. Contrib. Mineral. Petrol. 165 (4), 683–704.

Philpotts, A.R., Carroll, M., 1996. Physical properties of partly melted tholeiitic basalt. Geology 24 (11), 1029–1032.

Pin, C., Briot, D., Bassin, C., Poitrasson, F., 1994. Concomitant separation of strontium and samarium–neodymium for isotopic analysis in silicate samples, based on specific extraction chromatography. Anal. Chim. Acta 298 (2), 209–217.

Pouchou, L., Pichoir, F., 1984. A new model for quantitative X-ray microanalysis. Rech. Aérosp. 3, 167–192.

Ripley, E.M., Lightfoot, P.C., Li, C., Elswick, E.R., 2003. Sulfur isotopic studies of continental flood basalts in the Noril'sk region: implications for the association between lavas and ore-bearing intrusions. Geochim. Cosmochim. Acta 67 (15), 2805–2817.

Robert, J.L., 1976. Titanium solubility in synthetic phlogopite solid solutions. Chem. Geol. 17, 213–227.

Rodrigues, R., Soliani Jr., E., Takaki, T., Sato, K., Kawashita, K., 1997. Indicação cronoestratigráfica, com base em isótopos de estrôncio ($^{87}Sr/^{86}Sr$), das formações Andirá (Bacia do Amazonas) e cruzeiro do sul (Bacia do Acre). An. Acad. Bras. Ciênc. 69 (2), 173–178.

Schofield, N., et al., 2014. Mobilizing salt: magma–salt interactions. Geology 42 (7), 599–602.

Sobolev, A.V., Krivolutskaya, N.A., Kuzmin, D.V., 2009. Petrology of the parental melts and mantle sources of Siberian trap magmatism. Petrology 17 (3), 253–286.

Steinmann, M., et al., 1999. The corrosion of basaltic dykes in evaporites: Ar–Sr–Nd isotope and rare earth elements evidence. Chem. Geol. 153, 259–279.

Svensen, H., et al., 2004. Release of methane from a volcanic basin as a mechanism for initial Eocene global warming. Nature 429 (6991), 542–545.

Svensen, H., et al., 2009. Siberian gas venting and the end-Permian environmental crisis. Earth Planet. Sci. Lett. 277 (3), 490–500.

Svensen, H., Jamtveit, B., Banks, D.A., Austrheim, H., 2001. Halogen contents of eclogite facies fluid inclusions and minerals: Caledonides, western Norway. J. Metamorph. Geol. 19, 165–178.

Svensen, H., Aarnes, I., Podladchikov, Y.Y., Jettestuen, E., Harstad, C.H., Planke, S., 2010. Sandstone dikes in dolerite sills: evidence for high-pressure gradients and sediment mobilization during solidification of magmatic sheet intrusions in sedimentary basins. Geosphere 6 (3), 211–224.

Svensen, H.H., et al., 2018. Gondwana LIPs: plate reconstructions, volcanic basins and sill volumes. In: Sensarma, S., Storey, B.C. (Eds.), Large Igneous Provinces from Gondwana and Adjacent Regions. In: The Geological Society of London, Special Publications, vol. 463, pp. 17–40.

Teiber, H., et al., 2015. Equilibrium partitioning and subsequent re-distribution of halogens among apatite–biotite–amphibole assemblages from mantle-derived plutonic rocks: complexities revealed. Lithos 220–223, 221–237.

Tracy, R.J., 1991. Ba-rich micas from the Franklin Marble, Lime Crest and Sterling Hill, New Jersey. Am. Mineral. 76, 1683–1693.

Wanderley Filho, J.R., Travassos, W.A.S., Alves, D.B., 2006. O diabásio nas bacias paleozoicas amazônicas-herói ou vilão. Bol. Geoci. Petrobrás 14 (1), 177–184.
Wignall, P.B., 2001. Large igneous provinces and mass extinctions. Earth-Sci. Rev. 53, 1–33.
Willmore, C.C., Boudreau, A.E., Kruger, F.J., 2000. The halogen geochemistry of the Bushveld Complex, Republic of South Africa: implications for chalcophile element distribution in the lower and critical zones. J. Petrol. 41 (10), 1517–1539.
Yudovskaya, M.A., et al., 2018. Anhydrite assimilation by ultramafic melts of the Bushveld Complex, and its consequences to petrology and mineralization. In: Arribas, A.M.R., Mauk, K.L. (Eds.), Metals, Minerals and Society. In: Society of Economic Geologists Special Publication, vol. 21, pp. 177–206.
Zindler, A., Hart, S., 1986. Chemical geodynamics. Ann. Rev. Earth Planet. Sci. Lett. 14, 93–571.